Deformable Mirror Demonstration

Kristin Berry

Ashley K. Carlton

Zachary J. Casas

James R. Clark

Vladimir Eremin

Zaira G. Garate

Julian Lemus

Immanuel David Madukauwa-David

Tam Nguyen T. Nguyen

Paul Salcido

Alexandra E. Wassenberg

May 14, 2013

Contents

List of Figures

List of Tables

List of Acronyms

COTS Commercial off the shelf

DeMi Deformable Mirror Demonstration

DM Deformable Mirror

FOV Field of View

PSF Point Spread Function

ADCS Attitude Determination and Control System

IMU Inertial Measurement Unit

STK Satellite Tool Kit

1   Introduction - AW

Deformable mirror wavefront control systems correct for aberrations in the wavefront to produce high contrast images. This technology has been employed in ground telescope observation to counter wavefront distortions induced by Earths atmosphere. However, deformable mirrors have yet to be utilized on a space platform. Such an implementation could remove aberrations in the wavefront due to speckles from diffraction, noise, phase errors, and thermal drift. A proposed CubeSat Deformable Mirror (DeMi) demonstration will begin the process of testing adaptive optics technology in the space environment for future implementation on space telescopes and potentially free-space laser communication. The use of deformable mirrors in conjunction with coronographs onboard space telescopes will be able to produce images with higher achievable contrast in the direct imaging of exoplanets. This document presents a detailed overview of the role and design of the payload for the DeMi mission, a high actuator count MEMS deformable mirror yet to be tested in space, as well as the preliminary designs of the various satellite subsystems which support the flight of the payload in low Earth orbit.

1.1   Mission Statement

The mission of the Deformable Mirror Demonstration is to provide a low-cost, quick-access platform on which to demonstrate microelectromechanical (MEMS) wavefront control deformable mirror imaging technology (See Figure 1) on-orbit.
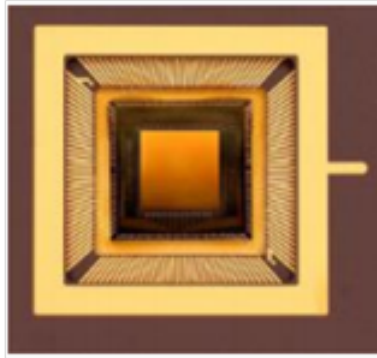
Figure 1: Boston Micromechanics MEMS Deformable Mirror [1]

1.2   Motivation

The driving force behind the DeMi mission is the desire to directly image Earth-like exoplanets in the search for signs of life, requiring imaging technology that can produce high contrast and dynamic range images. However, current high-performance space telescope technology suffers from wavefront aberrations, such as speckles which can result from diffraction, noise,

phase errors, and thermal drift and reduce the achievable image contrast.[2]

A solution to this problem is to implement adaptable wavefront control imaging technology in the form of a deformable mirror. In the deformable mirror system, a wavefront sensor measures wavefront aberrations in an approaching wavefront. An adaptive optics computer then calculates the errors in the wavefront reflecting off of the deformable mirror surface by subtracting the wavefront from a reference wavefront. [3] Finally, electrostatic actuators in an array beneath the membrane surface of the mirror individually deform the surface to correct the wavefront. A comparison of the effects of a flat and deformable mirror on an aberrated wavefront is demonstrated in Figure 2.
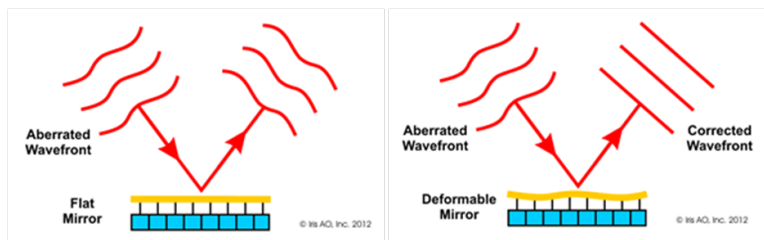
Figure 2: Comparison of the effects of a flat and deformable mirror on an aberrated wavefront

Adaptive optics technology is currently being used in conjunction with coronographs in ground telescopes to correct for distortions caused by Earths atmosphere and to resolve light from nearby objects. An example is seen in Figure 3 of three exoplanets imaged using the Palomar Observatorys Hale Telescope with adaptive optics technology. [4]

However, factors such as high speeds of atmospheric turbulence and limited numbers of photons from targeted exoplanets reduce the achievable image contrast. A solution to this issue is to incorporate deformable mirror wavefront control technology in high performance space telescope missions. The DeMi demonstration will take the initial step by testing the stability, calibration, and predictability of a more complex, higher actuator count deformable mirror system in space.

A space telescope utilizing a high performance coronograph and deformable mirror wavefront control system to directly image Earth-like exoplanets could potentially cost over a billion dollars. Therefore, a 3U CubeSat platform was selected to conduct the DeMi demonstration. The 3U CubeSat is a simple, standard platform, with low volume (10cm × 10cm × 30cm) and mass (maximum 4kg). CubeSats additionally have low manufacturing and launch costs and can provide relatively quick and easy access to space, as opportunities exist for them to fly as auxiliary payloads on rockets for other planned missions.

The technology that will tested in the DeMi demonstration has a number of foreseeable future applications, including implementation on high performance space telescopes, such as

---

[2]Cahoy, K. et al., CubeSat Deformable Mirror Demonstration, unpublished.

[3]Adaptive Optics Overview from Iris AO, Inc., http://www.irisao.com/technology.html.

[4]Serabyn, E., Mawet, D., Burruss, R., An image of an exoplanets separated by two diffraction beamwidths from a star. Nature, Vol. 464, 2010, pp. 1018-1020.
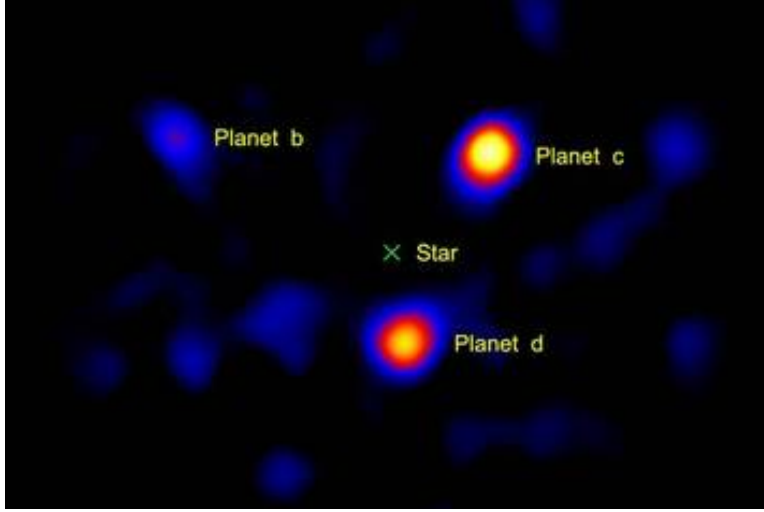
Figure 3: Three exoplanets directly imaged using a combination of adaptive optics and a coronagraph with the Palomar Observatorys Hale Telescope.

for direct imaging of Earth-like exoplanets, or for use with free-space laser communication in order to correct for aberrations in the atmosphere. [5]

2 Mission Overview

2.1 Requirements

See Appendix A.

2.2 Concept of Operations -ZG

DeMi will be a 3-unit CubeSat on a low-Earth orbit with an altitude of 500 km at an inclination of 40. Immediately separation from a standard Poly-PicoSatellite Orbital Deployer (P-POD), the satellite will begin to charge its primary batteries through solar panels covering the long faces of the structure. During this first stage, the satellites antenna will be deployed and will emit intermittent signals, or beacons, in order to be located by the ground station. The ADCS torque coils will detumble the satellite and align it in a nadir-pointing position. The detumble stage should last approximately 2 weeks. In case the satellite needs more time to power up, communicate with the ground station and stabilize itself, the science operations could be delayed.

Once the satellite is in fully operational status, the payload will begin to conduct its scientific experiments and collect data. Two different data capture modes will be performed during the mission: internal source experiments will be done during the first 3 months of

---

[5]Cahoy, K. et al., CubeSat Deformable Mirror Demonstration, unpublished.
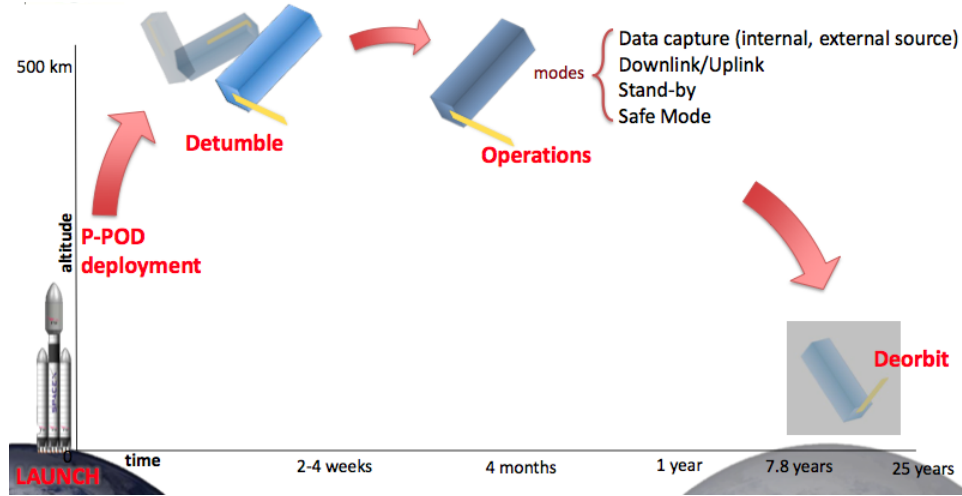
Figure 4: Timeline of the concept of operations for the DeMi Mission

operations, while external source experiments will occur during the remainder of the mission. The satellite will attempt to downlink the collected data whenever it passes over the NASA Wallops ground station and is given instructions to begin downlink.

The majority of the time, the satellite will be in stand-by mode; in other words, it will not be capturing or downlinking data. In case of a subsystem malfunction, the satellite will go into safe mode to diagnose the source of the problem.

Analyses performed using STK predict that the satellite will deorbit within 7.8 years. This timeline agrees with the current 25-year deorbit requirement outlined by NASA standards.2

2.3 N^2 Diagram

In the early stages of the design process, the team created an N^2 diagram to exchange input and output values. Additionally, this diagram became an essential tool in determining the levels of interaction between the satellites different subsystems.

As highlighted the figure above, the payload requirements drive the design of all the other subsystems. While it does not receive design inputs from other subsystems, its design outputs cascade down effectively driving the design of the rest of the satellite.

Feedback loops were present between several subsystems, which forced the team to perform trade studies to exchange performance for mass or power cost. One of these trades involved the design of the Power and ADCS subsystems. For example, complex solar panel designs that could absorb more solar energy, such as deployable panels, would require a more robust ADCS subsystem. However, such ADCS design would need to draw more power to maintain the panels facing towards the sun effectively cancelling the power gained. After careful consideration of costs and benefits, the team decided to take this option off the table

9

Payload	↘		↘	↘	↘	↘	↘
	Comm	↘	↘	↘	↘	↘	↘
	↑	Orbit	↘		↘	↘	
			Power	↘	↘	↘	↘
	↑		↑	ACDS	↘	↘	↘
	↑		↑		Avionics	↘	↘
			↑		↑	Thermal	↘
					↑	↑	Structures

Figure 5: High-Level N^2 diagram showing input/output relationships between subsystems

2.4   System Level Budgets

2.4.1   Mass

The mass budget is presented in Figure 6 below.

2.4.2   Power

The power budget is presented in Figure 7 below.

Figure 6: System Mass Budget
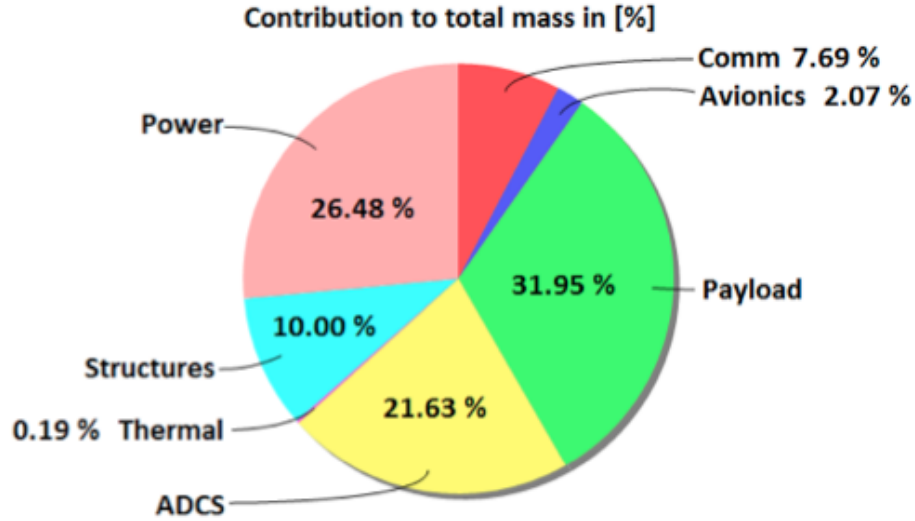
Mass Budget			
Subsystem	Mass Estimate (kg)	Margin[1]	Mass Budget (kg)
Structures	0.30	30%	0.39
Power	0.94	10%	1.03
ADCS	0.70	20%	0.84
Avionics	0.06	30%	0.08
Comm	0.25	20%	0.30
Payload	1.00	25%	1.25
Thermal	0.01	15%	0.01
Total	3.26	--	3.90

3 Subsystems

3.1 Payload

The payload for DeMi is an optical system that allows for the testing and technology demonstration of a deformable mirror system. It must include the following elements: the deformable mirrors the mission aims to test, a light source to create a wavefront, and a detector to measure the wavefront. These components are attached to an optical breadboard and are in an enclosure to block out external light. The challenge in this project is to create an optical system capable of testing the accuracy of current deformable mirror technology

Power with Margin Budget · Avionics · ADCS · Payload · Power · Comm
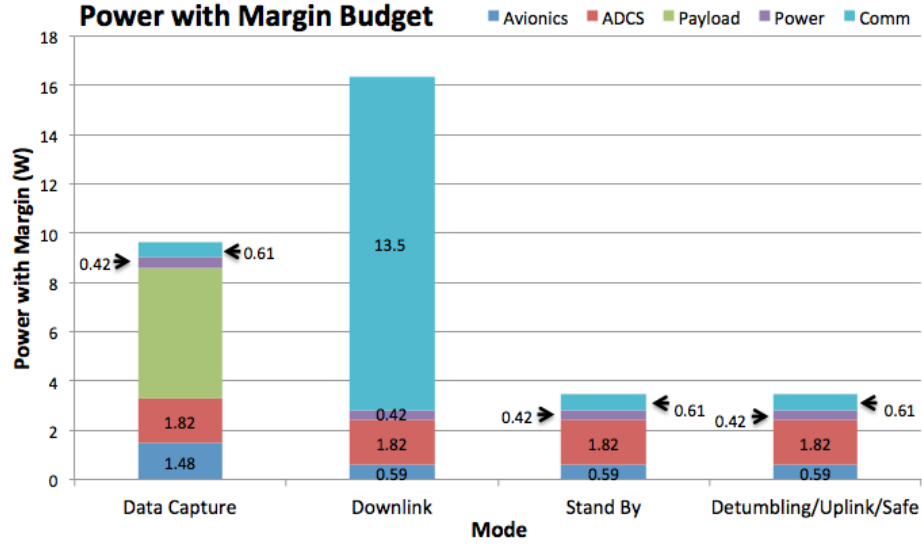
Power Budget			
Mode	**Duration [min/day]**	**Power [W]**	**Power [W] (with 18 % Margin)**
Safe/Uplink	--	2.92	3.44
Detumbling	~2 weeks	2.92	3.44
Data Capture	75	8.17	9.64
Downlink	46.7	13.84	16.33
Stand By	1318.3	2.92	3.44
Average	--	3.54	4.18
Power Supplied			3.84

Figure 7: System Power Budget

and evaluate its future applications while meeting the mass, volume and other constraints imposed by the 3U CubeSat platform.

3.1.1 Requirements - AC

There are two types of requirements on the payload. The first set (PLD-1) applies to the features of the deformable mirror system. The second set (PLD-2) pertains to the measurement and reconstruction of the wavefront. The complete requirements document can be found in Appendix A.

The requirements on measuring and reconstructing the wavefront (PLD-2) apply to the detector. Nominally, the detector must operate (capture images) for at least 5 minutes per orbit, and be able to function at a minimum of 10 Hz (PLD-2). The requirement is further separated into a "Diagnostic Mode" used for calibration and full frame images, and a "Burst Mode", used for data capture. In "Diagnostic Mode", the payload is required to take images

Table 1: Payload Requirements

PLD-1	The payload shall command a MEMS deformable mirror to run a pre-defined test sequence for at least 5 minutes each orbit. Parent Requirement: MLR-3, MLR-4
PLD-1.1	The payload shall have the ability to control any combination of actuators within 0.001 s of each other, at a minimum rate of 100 Hz, with a minimum stroke of 1.5 μm, and with a precision of at least 1 nm. Parent Requirement: PLD-1
PLD-2	The payload shall have the ability to measure and reconstruct the optical wavefront at one wavelength for the duration of a 5 minute test sequence each orbit at a frequency of at least 10 Hz. Parent Requirement: MLR-3, MLR-4
PLD-2.1	The payload shall have the ability to measure the optical wavefront at a minimum rate of 10 Hz for at least one minute each orbit. Parent Requirement: PLD-2
PLD-2.2	The payload shall have the ability to measure the optical wavefront at a minimum rate of 100 Hz for at least 30 seconds each orbit. Parent Requirement: PLD-2
PLD-2.3	The payload shall have the ability to reconstruct the optical wavefront with a minimum accuracy of 100 nm rms. Parent Requirement: PLD-2

for at least a minute per orbit at 10 Hz (PLD-2.1). In "Burst Mode", the payload is required to take images for at least 30 seconds per orbit a minimum of 100 Hz (PLD-2.2). For both modes, the reconstruction accuracy must be a maximum of 100 nm rms (PLD-2.3).

3.1.2 Decisions Made and Trade Studies

Payload Architecture - AC   While in future applications the deformable mirror system will be used to aid in observing stars or other objects, the mission goal of DeMi is to characterize the deformable mirror system, and to accomplish this with commercial off the shelf (COTS) components whenever possible, providing a quick and simple platform for space (MLR-3, MLR-4). As mentioned previously, there are a few key components that are integral to the design: the deformable mirror system to test, a light source to create a wavefront, and a detector to measure the wavefront. To keep the design as simple as possible, the use of an internal light source, such as a laser, is desirable for the technology demonstration.

Many techniques exist for measuring and reconstructing a wavefront [1]. These can be divided into sensored and sensorless approaches. Sensorless approaches, such as the Gerchberg-Saxton-Based Estimation Scheme [2], are likely to be used for a direct imaging application of a large space telescope mission for their ability to eliminate non-common path optical errors. However, sensorless approaches require additional computational resources, time, and occasionally additional detectors or detector translation [3]. Therefore, only sensored

approaches are considered for this platform due to the compact form factor, the desire to use simple COTS components, and processing capabilities. There are numerous wavefront sensing approaches that could be implemented, as well as modified versions of those presented here, but the two designs discussed are chosen for their ability to be simply implemented in a compact platform. While other designs (see Section 3.1.2) may be able to achieve higher precision, the Shack-Hartmann wavefront sensing system fits in the allotted volume with minor modifications to components, and allows for sufficient mirror characterization, meeting our mission goal and requirements (Table 1). Therefore, the Shack-Hartmann wavefront sensing design in Figure 8 has been chosen to image the wavefront.

Design Decision: Shack-Hartmann Wavefront Sensor - AC   For the wavefront sensing design in Figure 8, a Shack-Hartmann lenslet array is used, allowing for accurate wavefront measurement and reconstruction sensitivity. The design has an internal source (laser diode), whose path is denoted by a dotted red line, and an aperture for imaging an external source, whose path is denoted by a dotted green line.
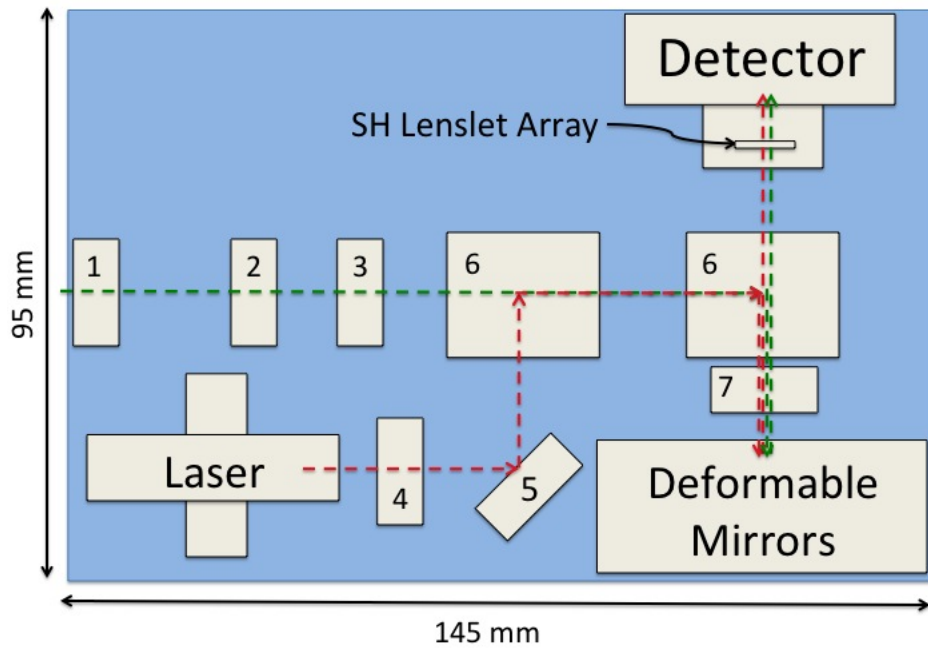
Figure 8: Design decision: Wavefront Sensing design with a Shack-Hartmann lenslet array

For the internal source, the laser diode module emits a collimated elliptical beam. This beam enters a linear polarizer (where its intensity is halved). The beam then encounters a flat mirror at 45 degrees, reflecting the beam 90 degrees, and proceeds to a primary beam splitter. Here, the beam is reflected 90 degrees to a secondary polarizing beamsplitter, and reflected another 90 degrees. The beam then goes through a quarter waveplate (where the

beam is now elliptically polarized) before striking the deformable mirrors. The deformable mirrors reflect the beam back through the quarter waveplate, rendering the beam now linearly polarized with an orientation that allows it to pass through the secondary beam splitter. The beam then proceeds through the lenslet array, creating a spot diagram on the detector corresponding to shape of the wavefront (see Section 3.1.2).

For the external source, the wavefront beam enters a plano-convex lens and passes through a collimating lens. The beam then enters a linear polarizer (where the intensity is halved). The beam passes through the primary beam splitter, and then to the secondary polarizing beamsplitter, which reflects the beam 90 degrees towards the quarter waveplate and the deformable mirrors, as mentioned previously, and follows an identical path as the internal light source to the detector.

The chosen design allows the detector to image both an internal and external source. While the mission goal can be accomplished with just an internal source, the ultimate goal of using this technology on a larger space telescope for imaging of bright stars motivates the use of an external source. Therefore, the option for an external source is included in the design.

Due to the added complexity required of the ADCS system on a CubeSat platform, the external source imaging will not require a precise star acquisition and navigation system. In contrast, with pointing knowledge from ADCS, the shutter on the aperture will be commanded open when a bright star is in the field of view (FOV). The maximum slew rate for imaging the external source is discussed in Paragraph 3.1.3. Based on preliminary models looking at five bright stars (Alpha Centauri, Arcturis, Canopus, Sirius, and Vega), the satellite would expect to see the same bright star every orbit for an average of three to five minutes[6]. The pointing requirement on the maximum ADCS slew rate to keep the star on the same pixel on the detector is discussed in Section 3.1.3.

It is necessary that the aperture for imaging an external source be small, given the volume constraints of the CubeSat platform after accommodating all of the key elements of the system (deformable mirror, mirror driver electronics, detector, and necessary imaging optics). Due to the physical size of these key elements, it is not practical to design the external source imaging as a typical reflecting telescope. While it may be possible to accommodate an aperture lens with relatively large diameter (> 60 mm), the corresponding longer focal length would not fit in the volume, and the space for resizing the beam is limited. While the smaller aperture will limit the angular resolution and sensitivity and increase the size of the point spread function (PSF), tight angular resolution is not a requirement for this technology demonstration. Therefore, this design has an aperture lens with diameter 12.7 mm, with a minimum focal length on the order of its diameter. Using the Rayleigh criterion, the angular resolution (width of the center of the PSF) at 500 nm is 9.907".

The current design allows for open and closed loop control. Images and centroid solutions can be sent to the ground, allowing for evaluation of the mirror performance over time. In addition, closed loop control (active correction of the wavefront on orbit) can also be implemented on board using the centroids and calculated slopes to command the mirrors.

---

[6]Based on an STK simulation performed by Annie Marinan.

Calculating mirror response from slopes requires little additional processing [8].

All optical elements of the system are preliminarily chosen. (See Appendix **??** for the full list of elements with part numbers and mass totals.) Glass elements are chosen to be UV fused silica over other glasses whenever possible for their better performance in space [4] due to a high coefficient of thermal expansion and better UV transmission. All elements also have anti-reflective coatings that are efficient in the visible spectrum (400 - 700 nm). All components in Figure 8 are shown with their mounts. However, the mass and volume of the mounts are only estimates of the custom mounts that will be built for all optics. Custom mounts will be built to adapt the optics for space applications. All elements must be mounted in stress-free mounts (e.g., no glass touching metal) and mounted to an optical breadboard with multi-footed lens tubes that are made of aluminum, or of a metal that has a similar coefficients of thermal expansion as the lens it holds. Future modeling and optimization of the optical design will yield more exact component choices.

Other Designs Considered: Michelson Interferometer with Nanopositioner - AC The interferometer design shown in Figure 9 is slightly modified from a typical interferometer due to volume constraints on the payload and the requirement for high contrast imaging. It has an internal source (laser diode), whose path is denoted by a dotted red line. The laser beam is first resized, passes through a neutral density filter, then is reflected 90 degrees by a flat mirror. The light is then divided by a beam splitter oriented 45 degrees to the beam. The transmitted beam travels to the deformable mirror where it is reflected back towards the beam splitter. Half of the beam is deflected by 90 degrees at the beam splitter and strikes the detector. The reflected beam travels to the flat mirror on the nanopositioner where it is reflected and half of it then is transmitted through the beam splitter and reaches the detector. The two beams that reach the detector interfere to produce fringes [5] that are analytically well understood as a function of beam coherence/divergence and mirror tip/tilt [6] and that can be simulated for a variety of different deformable mirror shapes.

For this particular design, as mentioned previously, a flat mirror is on a nanopositioner, or a piezo linear stage, which moves in increments of fractions of the incoming wavelength. This allows for higher precision fringe patterns, allowing for better mirror characterization.

What is not shown in Figure 9 is the controller for the nanopositioner [7]. It does not currently fit within the constraints of the satellite in terms of mass, volume, and power needs, and would require significant modifications, if it were to be implemented. Also, the additional moving part (nanopositioner) increases the risk and complexity of the mission, making the Shack-Hartmann wavefront sensor the design choice.

Payload Operations - AC For the initial demonstration and on-orbit testing, an internal light source will be used. This eliminates any payload specific requirements on the satellite's attitude and inclination. For the latter half of the mission, an external light source will be used, in order to attempt to image the optical wavefront from a star. All downlinked files will be timestamped.
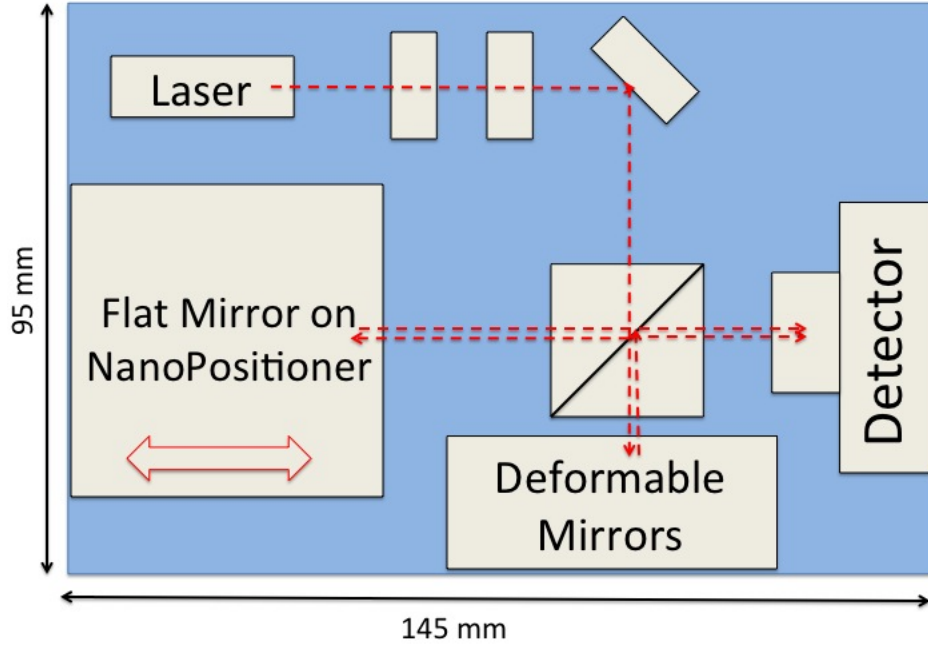
Figure 9: Other considered design: Michelson Interferometer with the flat mirror on a nanopositioner.

1. **Status Checks** After detumbling, and two weeks of commissioning, as describe in Section **??**, the payload will perform a status check of all instruments. This includes the deformable mirror system, the detector, and the laser. Each element will be turned on and checked for error or status codes. Any available status information directly from the deformable mirrors, detector, and laser will be sent to the ground.

2. **Calibration** The next phase is to calibrate the system using the "Diagnostic Mode" requirements outlined in Section 3.1.1. This involves turning on the laser and recording several images in this configuration with the detector, without deforming the mirrors (acts as a flat mirror). From these images, on-board processing algorithms can find the centroids [8] and average them to obtain new 'standard centroids', which will be used for wavefront comparison calculations throughout the remainder of the mission. These images, averages, and new centroid solutions will be sent to the ground and stored on-board.

3. **Data Capture: Internal Source** The next, and most important, stage is data capture using the internal source. The laser is turned on, then the mirror is deformed by a predetermined test sequence of commands, and the wavefront is imaged on the detector. The test sequence will include 'poking' one actuator at a time, and 'poking' combinations of actuators in commonly known shapes, such as Zernike polynomials and Fourier modes. Then, the images are read from the detector, centroids are found, and

17

one full image and the collection of centroid solutions are sent down to the ground and stored on-board. Local wavefront slopes will be found from the centroid solutions using simple on-board algorithms, and the mirrors will be commanded for active wavefront correction on-board.

4. **Data Capture: External Source** The second part of data capture will be with an external source. This external source will be a bright star, such as Vega or Sirius, as mentioned previously. With knowledge from ADCS, the shutter will be commanded open, and the laser will be commanded off, allowing an external source to be imaged. The images will be read from the detector, the centroids found, and one full frame image along with the collection of centroid solutions will be sent to the ground and stored on-board. Identical to data capture with an internal source, local wavefront slopes will be found from the centroid solutions using simple on-board algorithms, and the mirrors will be commanded for active wavefront correction on-board.

Deformable Mirror System - KB There are only two vendors which sell commercial off-the-self options for MEMS deformable mirrors that will fit inside a CubeSat: Boston Micromachines, and Iris Adaptive Optics. The Boston Micromachines Mini DM comes in three different sizes of stroke and aperture. Stroke referes to the maximum amount the mirror can 'push' a segment outward, and the aperture is simply the aperture of the DM. Since there is little room for resizing optics in our system, the aperture of the DM acts as a stop. As such, larger apertures are strictly better for the accuracy of the wavefront we can reconstruct. While the Iris AO PT111 does have a larger aperture *and* a larger stroke, which are both better for accuracy, its driver board is larger and much more difficult to modify than the BMC Mini's. As such, we selected the largest BMC mini DM, with a 2.25 mm aperture and a stroke of 5.5 μm.

Detector - KB For a detector, we chose the UI52-41LE-M CMOS detector from IDS. Critically, it has a 5.2μm pixel size, which is smaller than the pixel sizes we looked at for the alternatives. Since accuracy is a function of pixel size, maximizing pixels per subaperture is very important. Alternatives we considered included the DCC1545M and the e2v CCD47-20 frame transfer CCD (Table 2).

Table 2: This needs a caption.

Detector	Req. PLD-2	47-20	DCC1545M	UI1221LE-M	UI5241LE-M
Manufacturer	-	e2v	Thorlabs	IDS	IDS
Type	-	Frame transfer CCD	CMOS	CMOS	CMOS
Full frame rate	10 Hz	5 MHz	25 fps	87.2 fps	50 fps
Subframe rate	100 Hz	-	79 fps	100 fps	102 fps
Accuracy	100 nm rms	11.2 nm rms	45 nm rms	45 nm rms	45 nm rms
Data Rate	-	52.4 Tbit/sec	259 Mbit/sec	207 Mbit/sec	310 Mbit/sec

Shack-Hartmann Lenslet Array - AC A Shack-Hartmann lenslet array consists of a matrix of small lenses (called lenslets) of the same focal length, where the array is focused on the detector. Each lenslet forms a spot, creating a spot diagram on the detector. Figure 10 demonstrates incoming light through a lenslet array. The local tilt of the wavefront across each lenslet can then be calculated from the position of the focal spot on the sensor; the displacement, Δx, equals the local slope of the wavefront. Any phase aberration can be approximated to a set of discrete tilts. By sampling an array of lenslets, all of these tilts can be measured and the whole wavefront approximated. Only tilts are measured, so the lenslet array cannot detect discontinuous steps in the wavefront.
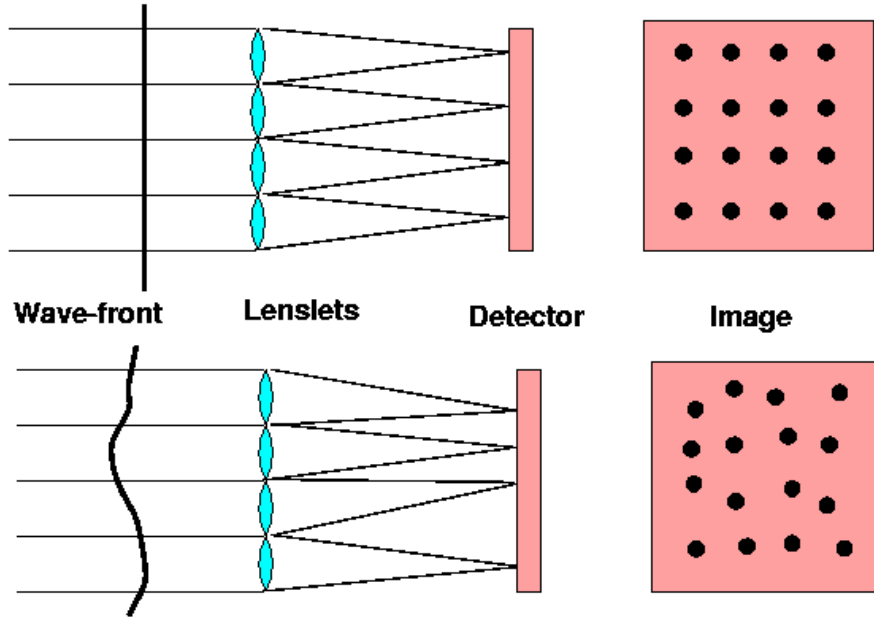
Figure 10: The result of two wavefronts, plane (top) and abberated (bottom), entering a Shack-Hartmann lenslet array, and their resulting spot diagrams on the detector [9].

To get the best measurement of the wavefront, the maximum number of spots, and therefore lenslets, is desired. As a result, for a constant beam size, a lenslet array should be chosen with the lowest pitch (distance from the center of each lens) in order to get the maximum number of spots for the beam.

Therefore, the microlens array MLA150 was chosen from ThorLabs [10] (see Figure 11), with a pitch of 150 μm. The lenslet is 10 mm square, so it contains about 66 by 66 lenslets. It is mounted in the lens tube on the detector. For an approximate beam size of 2.25 mm (see Paragraph 3.1.2), approximately 15 by 15 lenslets will be used of the lenslet array. See Section 3.1.3 for a discussion of the pixels used on the detector per lenslet.

3.1.3 Analysis - KB

Figure 11: The MLA150 lenslet array from ThorLabs [10] chosen for the Shack-Hartmann Wavefront Sensing design consists of many microlenses, aligned closely together.

Pointing Requirement - KB

Data Rates to Avionics - KB

Shack-Hartmann Lenslet Array - AC

Pixels per Lenslet Spot   In order to image the spots created by the Shack-Hartmann microlenslet array, spots must fall on their own unique pixels. At least four pixels are required per lenslet spot (a two by two square of pixels) to account for the event in which a spot lands between two pixels, or at the center of four pixels. The incoming beam is 2.25 mm (Paragraph 3.1.2). This corresponds to about 15 by 15 spots. The detector has a pixel size of 5.2 μm, so a 2.25 mm beam corresponds to about 425 px square. Therefore, over twenty pixels are available for each lenslet spot, so there is no concern for multiple spots falling on the same pixel.

Actuators per Lens   The chosen BMC deformable mirrors have a total of 32 actuators (a 6 by 6 array, with no corners) with an actuator pitch of 450 μm [11]. The Shack-Hartmann

Table 3: Summary of the mass totals, power needs, and thermal needs of the major payload components.

Component	Mass (g)	Power (W)	Thermal, operating (°C)	Thermal, storage (°C)
Laser diode	24.45	0.0045	-10 to 50	unknown
Detector	46.64	< 2 W	0 to 50	-20 to 80
Def. Mirrors + Driver	189.9	< 2.5 W	-10 to 50	unknown
Optical Breadboard	~250	–	–	–
Optical Enclosure	~300	–	–	–
Totals	996.9	4.5 W max	0 to 50	-20 to 80

lenslets have a pitch of 150 μm, so there will be a minimum of four spots devoted to each actuator. Therefore, there is no concern for individual actuators to be untested or characterized properly.

3.1.4 Summary of Outputs - AC

The payload's operational requirements are major drivers for the design of the rest of the satellite. A summary of mass totals, power needs, and thermal requirements of all major payload components can be found in Table 3. During data capture mode, the payload must be kept within 0°C to 50°C, will draw a maximum power of 4.5 W, will output a maximum data rate of 550 Mbit/s, and, during external data acquisition only, has a maximum slew rate of 4.7'/s. With all components, the payload is 1.00 g, and 1.25 kg with a 25

3.1.5 Future Work - AC

Future work includes optical modeling of the system using the software ZEMAX [12]. Modeling the system with ZEMAX will determine the final beam profile on the detector. This will allow for more precise calculations of data rates, for example. Optimization of the space will be determined to find the best choice of components. Thermal effects on the beam and optical components will be also analyzed, along with the effects of slight misalignments (i.e. with lenslet array).

Also, to determine the feasibility of the interferometer with the nanopositioner design, discussions with various nanopositioner manufacturers are needed to resolve if the nanopositioner elements can be appropriately modified for a CubeSat platform. Preliminarily, a nanopositioner would require additional power and processing. Further effects on other subsystems needs to be determined.

Furthermore, while the design allows for imaging of an external source, when and how to image an external source still needs to be determined. Specific bright stars need to be chosen, and their revisit times calculated more precisely based on the orbital parameters unique to DeMi.

Lastly, specific properties of the deformable mirror system need to be explored. For example, a stroke analysis needs to be performed. Also, research needs to be done to try to

predict the deformable mirror system's performance in a space environment, and how this might be quantified and corrected.

3.2 Power - JC

3.2.1 Requirements

The Power subsystem is required to supply power to all other subsystems under all conditions. In particular, it must supply an average of 3.54 watts on average over the course of the orbit (calculated in Section 3.2.4, Analysis), sustain a maximum load of 13.84 watts during certain operational modes (downlink mode, per Systems), have a minimum battery capacity of 3.9 watt-hours (calculated in Section 3.2.4, Analysis), and meet these requirements for up to 1 year, or approximately 6,000 cycles (calculated in Section 3.2.4, Analysis).

3.2.2 Trade Studies and Decisions Made

Using STK, we compared the average power obtained by the solar panels under several circumstances. The two variables were the inclusion or omission of a solar panel on the top face of the satellite, in addition to the four side-mounted panels, and the orientation of the satellite in its orbit – whether it few "face-first", with the normal vector of one of its sides aligned with its velocity, "corner-first", where it is tilted by 45 degrees about its long axis from the face-first orientation, or spinning about its long axis. The face-first and corner-first attitudes are illustrated below:
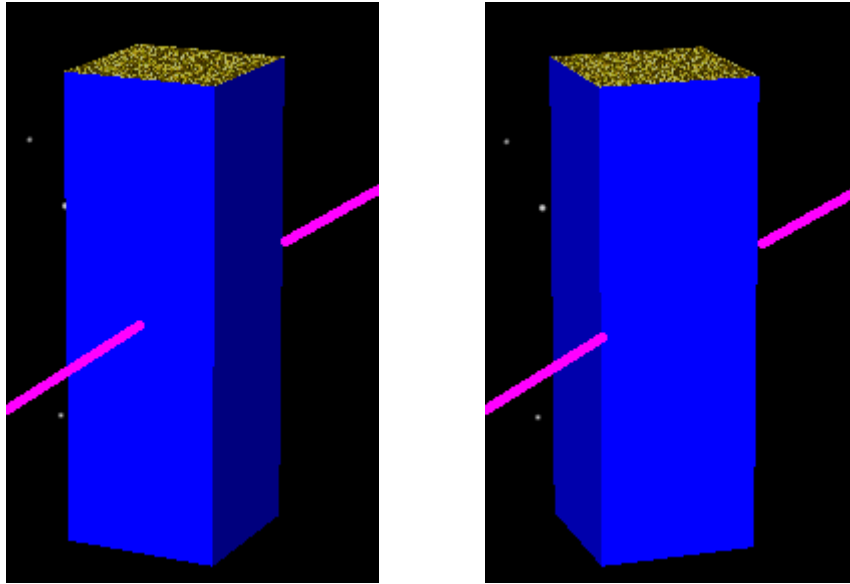
Figure 12: The "face-first" and "corner-first" attitudes. Images generated from STK.

Note that these power values are averaged over the entire orbit – that is, taking the incoming power to be zero during local night and including that in the average. This was done because the satellite is active during the entire orbit, and its average power needs are calculated over the entire orbit; to ensure that we are comparing likes against likes, we did the same for the power generated.

Table 4: Power values for various panel configurations and satellite attitudes.

	Face-first	Spinning	Corner-first
Side panels	3.77 W	4.16 W	4.52 W
Side and top panels	4.45 W	4.84 W	5.19 W
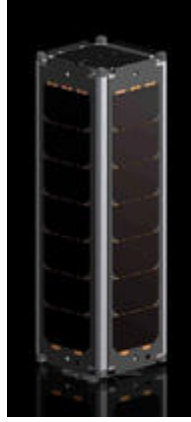
Figure 13: The solar panel configuration to be used on the DeMi satellite. Image from Clyde Space.[15]

3.2.3 Decisions Made

In general, the power subsystem was designed to be as simple as possible while meeting the satellite's power needs. We chose to use stock parts as much as possible because they have known performance, which helps us verify that requirements are met and reduces the margins we need to hold.

The chosen solar panel configuration was four body-mounted side panels. Body-mounted panels were chosen over deployable panels because they minimized the surface area of the satellite, which minimized the disturbance torques, and they are symmetrical, reducing the pointing constraints on the ADCS. The satellite would be oriented in a nadir-pointing configuration, so the nadir face would almost never see any sunlight, so we chose not to panel it, and we chose not to panel the zenith face to allow the payload to have an aperture in that face, so that it could potentially image external light sources.

The remainder of the power system is similar to that of most other satellites: an electrical power system module takes power from the solar panels and manages the current and voltage levels to ensure that the panels deliver power at maximum efficiency, a secondary (rechargeable) battery supplies the satellite with energy during eclipse, and a power distribution module supplies power to systems which are not part of the main system stack, like the torque coils.

The satellite's power subsystem does not include a primary battery. A primary battery was never included in the design because the satellite was to be covered on most sides by

solar panels and would be power-positive in detumbling mode, so it would charge as soon as it exited the P-POD. The only reference to a Cubesat containing a primary battery was a description of a Cubesat that lacked solar panels entirely.[16]

3.2.4 Analysis

The average power required is the time-weighted average of the power required during the various modes of the satellite:

$$P_{req,avg} = \frac{1}{T_{total}} \sum_{modes} \sum_{systems} T_{mode} \, P_{sys,mode} = 3.54 \text{ W} \tag{1}$$

The solar panels are required to gather enough power during the day to power the satellite for the entire orbit, when taking the inefficiency of the EPS into account ($\eta = 0.85$ in the worst case[17]):

$$P_{req,panels} = \frac{T_d + T_e}{T_d} \frac{P_{req,avg}}{\eta} = 6.61 \text{ W (cold)}, 5.21 \text{ W (hot)}, 4.16 \text{ W (orbit avg)} \tag{2}$$

"Hot" and "cold"[7] here refer to the two orbital cases which have the most and least solar exposure for the satellite because the orbit is fixed in inertial space, it appears to rotate with respect to the Earth-Sun vector over the course of a year. Every six months, it goes from a cold orbit, which is in the sunlight 63% of the time, to a hot orbit, which is 80% sunlit, and back again. The two orbits are illustrated below.

The satellite drains the most energy from the battery if it performs a ground station pass (maximum duration: 9.77 minutes, per Comm) and scientific operation (nominal duration: 5 minutes, per Payload) during local night:

$$E_{req,batt} = T_{sci}P_{sci} + T_{comm}P_{comm} + (T_e - T_{sci} - T_{comm})P_{standby} = 3.9 \text{ Wh} \tag{3}$$

The excess power is the power actually generated by the panels that does not go into powering the satellite or charging the battery – in other words, the difference between the power required power and the power actually generated:

$$P_{excess} = P_{panels} - P_{req,panels} = 0.63 \text{ W (cold)}, 2.57 \text{ W (hot)} \tag{4}$$

It can be useful to model the excess power as an average over the entire orbit, rather than just happening during local day (for first-order approximations of the equilibrium satellite temperature):

$$P_{excess,avg} = P_{excess} \frac{T_d}{T_d + T_e} = 0.40 \text{ W (cold)}, 2.06 \text{ W (hot)} \tag{5}$$

---

[7]Perhaps "bright" and "dark" would be better terms from a power perspective, because it is not temperature that gives us power but sunlight.
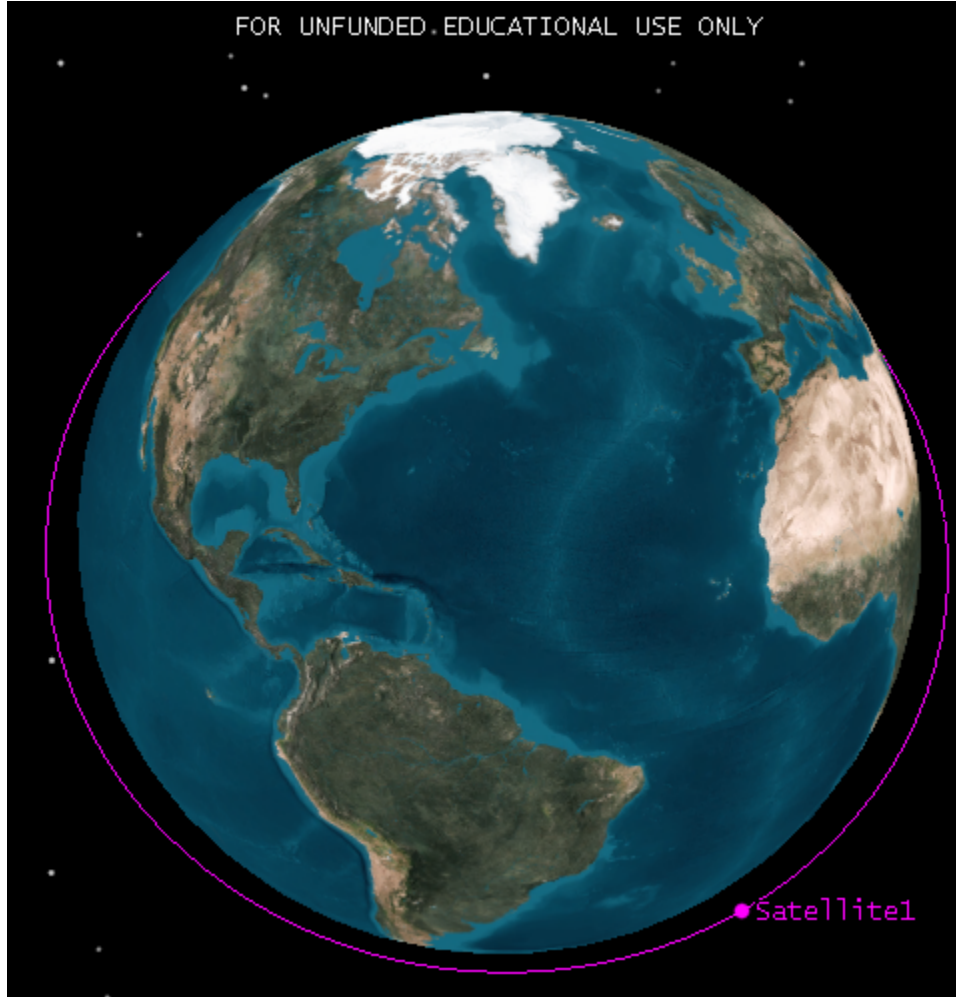
Figure 14: A "hot" orbit, where the satellite is exposed to the sun 80% of the time. Image generated from STK.

The number of charge-discharge cycles of the battery is approximately equal to the number of orbits that the satellite will have to sustain:

$$N_{cycles} = \frac{T_{year}}{T_{orbit}} = 5500 \approx 6000 \text{ (with 10\% margin)} \tag{6}$$

3.2.5 Summary of Outputs

The solar panels do not literally have zero volume, but because they are fixed to the sides of the Cubesat, they do not occupy any of the three units of internal volume.
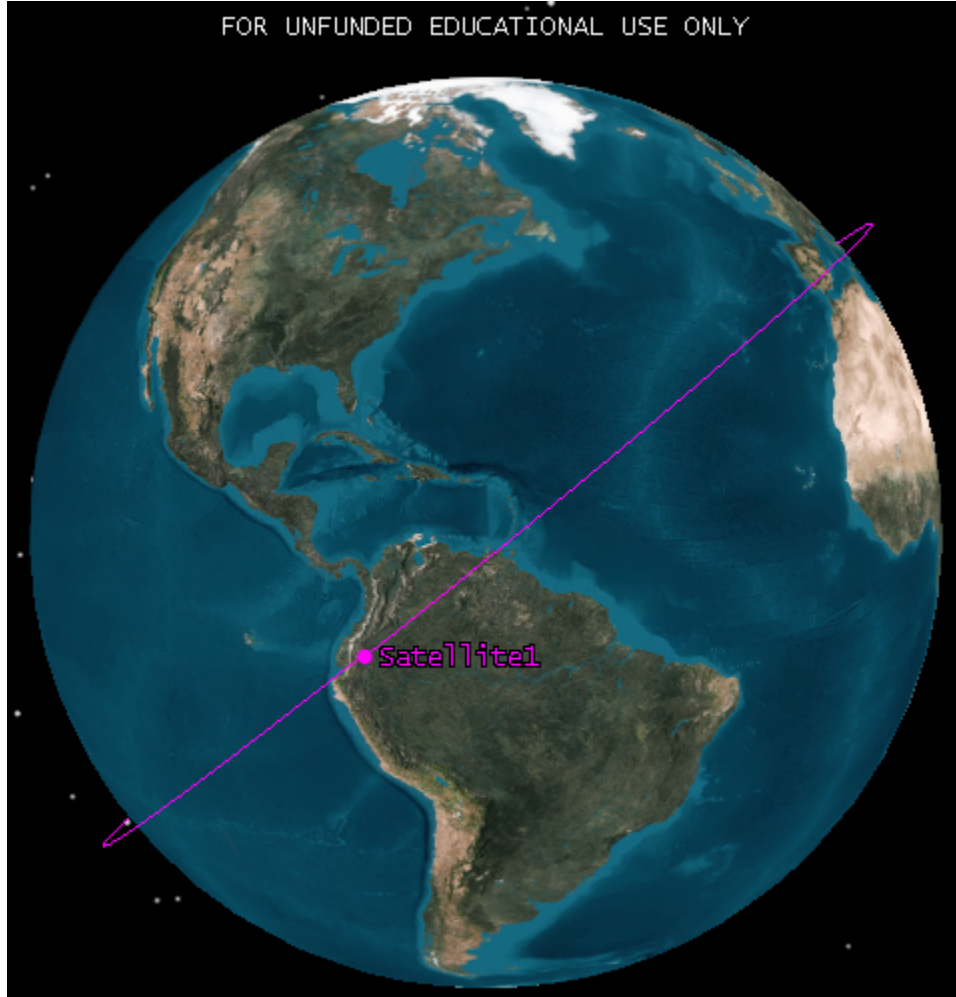
Figure 15: A "cold" orbit, where the satellite is exposed to the sun 63% of the time. Image generated from STK.

3.2.6 Risks

The primary risk facing the Power subsystem is that our incoming power is fundamentally limited, so we will have to be careful to not exceed our budget. As computed in Analysis (Section 3.2.4), the average power drawn by the satellite for nominal mode durations is 3.54 watts. While the orbit-averaged power coming in from the solar panels is 4.52 watts, which is a 28% margin over the power needs, when we take the worst-case efficiency of the EPS's solar-panel connection into account[17], we find that as little as 3.84 watts are actually getting to the battery power bus, leaving only a 9% margin (which might then be further eroded by inefficiencies in the power lines). This is less than the 18% margin goal we had set for ourselves, and substantially less than the 30% margin that JPL informed us was their usual standard for satellite missions.

This risk is mitigated by the 32% margin of available power over the standby power need of

Table 5: Outputs to other systems (mass, volume, power consumed, and survival and operating temperatures).[17] [18] [19] [20]

Component	Mass (kg)	Volume (U)	Power consumed (W)	Survival temperature (° C)	Operating temperature (° C)
Solar panels	0.540	0	0	-40 to 80	-40 to 80
EPS	0.083	0.15	0.1	-50 to 100	-40 to 85
Battery	0.256	0.2	0.1	-10 to 50	0 to 50
PDM	0.060	0.25	0.16	-50 to 100	-40 to 85
Total	0.939	0.6	0.36	N/A	N/A

2.91 watts. From this, we can be confident that, even in the worst possible case, the satellite will be power-positive during its standby mode. This means that, if the satellite should find itself unable to meet its power needs for nominal mode durations, it could be commanded to spend more time in standby mode and less in data capture or downlink mode to restore balance to its power budget. As mentioned in the Analysis section, the available power was calculated for the coldest, darkest orbit that the satellite will be in. For the brightest orbit, the average power generated by the solar panels over the entire orbit increases to 7.42 watts, which, taking the worst-case EPS efficiency into account, results in 6.31 watts reaching the power line, which is a 78% margin over the average power required. In fact, we could spend 29 minutes – nearly six times the nominal data capture mode duration – of such a bright orbit in data capture mode (leaving the downlink mode duration constant, as ground pass durations are independent of available power) while maintaining a 30% margin of available (post-EPS) power over required power. We can thus be assured that, even if the satellite is forced to reduce the duration of data capture and downlink modes during darker orbits to conserve power, we can make up for any shortfalls of captured data during better orbits.

3.2.7   Future Work

The performance of the solar panels and batteries is temperature-dependent. In particular, the battery becomes more effective as its temperature increases, while the solar panels become less so. Going forward, it would be useful to perform a more detailed simulation of the satellite that incorporates a thermal model, so that we can more accurately measure the effect of satellite temperature and dissipated excess energy (energy from the solar panels that does not go into charging the battery or powering the satellite).

3.3 Communication

3.3.1 Requirements - ZC

Table 6: Communications Driving Requirements

COMM-3.1	The subsystem shall transmit at 19.2 kb/s for uplink and 1.5 Mb/s for downlink. Parent Requirement: COMM-3
COMM-3.2	The subsystem shall have a bandwidth of $445 - 455\ MHz$ for uplink and $460 - 470\ MHz$ for downlink. Parent Requirement: COMM-3

The driving requirements for the communications subsystem are that it should transmit at the data rates and frequencies (Comm-3.2) that are necessary to transmit all data to the ground station. The required frequencies are $445 - 455\ MHz$ for uplink and $460 - 470\ MHz$ for downlink. The required data rates are 19.2 kb/s for uplink and 1.5 Mb/s for downlink.

3.3.2 Decisions Made - ZC

The L-3 Cadet Nanosat UHF Radio was chosen for use on DeMi. It transmits at the frequencies and data rates outlined in the requirements. The transceiver has an extra 4 GB of storage that avionics uses in addition to any of its storage.

Because the transceiver is transmitting and receiving at UHF frequencies, a very common antenna choice is to use a measuring tape antenna that is tuned to the frequency that is desired. Because the antenna works like a quarter-wave monopole, the desired length of the antenna is calculated by dividing the wavelength of the signal by 4. Because the transmitting and receiving frequencies are different, the average of these frequencies is used to compute the wavelength. With a frequency of 465 MHz, the wavelength equals .645 meters. Then, the length of the antenna can be determined using Eq. 7.

$$\lambda = c/f \tag{7}$$

In Eq. 7, l is the length of the antenna, and λ is the wavelength. Using a wavelength of .645 meters, the desired length of the antenna is about .164 meters. The gain of this antenna will be approximately 3 dB and the beam width approximately 65°. DeMi is using two of these antennas so that communication can occur even if it is rotated 180 degrees from where it is supposed to be.

The ground station that DeMi communicates with will be the NASA Wallops UHF Ground Station. This ground station is being used because the transceiver chosen for DeMi was also used in the Dynamic Ionosphere CubeSat Experiment, and the ground station that was used in that mission was the NASA Wallops UHF Ground Station. The diameter of the dish is 18.29 meters, the gain is 35 dB and the beam with is 2.9°.

3.3.3 Trade Studies - ZC

The main factor in choosing the transceiver on DeMi is the maximum data downlink rate. Because payload is generating so much data, the communications system needs to have a high downlink rate to ensure that all of that data can be sent to the ground. Several options were investigated, and the transceiver with the highest data rate is being used. The transceivers that were considered and their maximum data rates are shown in Table 7.

Table 7: Communications Trade Study for Maximum Downlink Data Rate

Tranceiver	Maximum Downlink Rate
Espace Payload Telemetry System	1 Mb/s
AstroDev Li-1 UHF Transceiver	38.4 kb/s
ISIS TXS Small Satellite S-Band Transmitter	100 kb/s
Tyvak UHF Transceiver	200 kb/s
L-3 Cadet Nanosat UHF Radio	1.5 Mb/s
Microhard MHX2420 Modem	230.4 kb/s

3.3.4 Analysis - ZC

The maximum amount of data downlink per pass-by can be calculated by multiplying the downlink data rate and the access duration per pass-by. Given the downlink data rate of 1.5 Mb/s, and the access duration of 586 seconds per pass-by, the maximum amount of data that can be downlinked in one pass-by is 109.9 MB. Because the satellite is not always directly above the ground station, the satellite is not always downlinking at the maximum data rate. To account for this, and for space for telemetry data and error correcting code, a margin of a factor of 2 is added, so the maximum amount of data from payload that can be downlinked per pass-by is about 54.95 MB. Although this is not as much data as payload is creating, on-board processing is used so that the amount of data that needs to be downlinked is below the maximum amount that is allotted for payload.

A link budget was created in order to determine the link margin for a worst case and a best case for uplink and downlink. The uplink budget and the downlink budget are detailed in Appendix B.

The first calculation for the link budget is to determine the worst case propagation path length. The best case length is 500 km because that is the altitude at which the satellite is orbiting. Figure 16 shows how a wave propagates through that atmosphere.

In order to determine the propagation path length, r, the path length of the first layer and the second layer must be determined and added together. The equation for calculating the path length of a layer is as follows in Eq. 8 [21, p. 9].

$$a_n = -r_n \cos(\beta_n) + \frac{1}{2}\sqrt{4r_n^2 \cos^2(\beta_n) + 8r_n\delta_n + 4\delta_n^2} \tag{8}$$
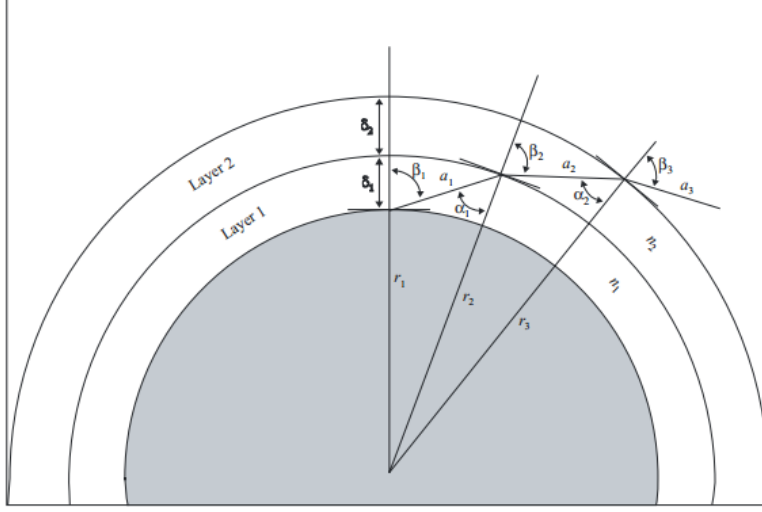
Figure 16: Diagram of propagation path of a signal from a satellite [21, p. 12].

In this equation, a_n is the path length through layer n, r_n is the radius from the center of the Earth to the beginning of layer n, β_n is the exiting incidence angle, and δ_n is the thickness of layer n. The angle β_n can be calculated using Eq. 9 [21, p. 10].

$$\beta_{n+1} = \arcsin\left(\frac{n_n}{n_{n+1}}\sin(\alpha_n)\right) \tag{9}$$

In this equation, n_n is the refractive index of layer n, and α_n is the entry incidence angle. Angle α_n can be calculated with the last equation needed in order to calculate the propagation length, Eq.

$$\alpha_n = \pi - \arccos\left(\frac{-a_n^2 - 2r_n\delta_n - \delta_n^2}{2a_nr_n + 2a_n\delta_n}\right) \tag{10}$$

Values that still need to be defined are β_1 (because it cannot be calculated using the Eq. 10), δ_1, δ_2, n_1, and n_2. β_1 is just equal to the complimentary angle to the minimum angle at which the Wallops Ground Station can track, which is 5°. δ_1 will be equal to the altitude at which the atmosphere ends which one can say is about 100 km. δ_2 is just the orbiting altitude minus δ_1. n_1, which is simple the refractive index of air, is 1.000293. The last remaining value to be defined is n_2, which is the refractive index of a vacuum, which is just 1. Using these equations, one can find that a_1 equals 707 km, and a_2 equals 1375 km. This means that the worst case propagation path length is equal to 2082 km. The refraction of the wave in air did not change the path length by very much. Without accounting for the refraction, the path length can be calculated using the equation for a_n. In this calculation, r_n equals r_1, β_n equals β_1, and δ_n equals 500 km which is the altitude at which DeMi orbits. These values give a path length equal to 2077 km, which is only 5 km shorter than the path length when taking refraction into consideration.

The next value calculated in the link budgets is the Equivalent, Isotropic Radiated Power (EIRP). In order to calculate the EIRP, Eq. 11 should be used [29, p. 476].

$$EIRP = P_{tx} + G_{tx} - L_{output} \tag{11}$$

In Eq. 11, P_{tx} is the transmitter power, G_{tx} is the transmit antenna gain, and L_{output} is the output loss which is equal to all losses associated with the transmitter. All of these values can be found in the two link budgets in Appendix B.

Another calculated value in the link budget is the space loss. This is the loss of the signal as it is transmitted through space. It can be calculated using Eq. 12 [29, p. 476].

$$L_s = 92.45 + 20\log_{10}(r) + 20\log_{10}(f) \tag{12}$$

In Eq. 12, L_s is space loss, r is the propagation path length, and f is the frequency of the transmitted signal. All of these values can also be found in the two link budget tables in Appendix B.

Eq. 13 can be used to calculate the transmitting antenna temperature [22].

$$T_{antenna} = \eta T_{sky} + (1 + \eta)\frac{T_{sky} + T_{ground}}{2} \tag{13}$$

In Eq. 13, η is the antenna efficiency, T_{sky} is the temperature of the space behind the receiving antenna. The temperatures used for uplink are determined by using the background temperature of space. For downlink, the temperature of the Earth is used. T_{ground} is the temperature of the ground around the antenna. For uplink, this is the temperature of the Earth, and for Downlink, it is the background temperature of space.

The system noise temperature, T_{sys}, is calculated by adding the transmitting antenna temperature and the receiver temperature [22]. The receiver temperature for both cases is unique to the receiver and can be determined by the manufacturer.

The next calculated value is the Receiver Gain to Noise Temperature. This is computed using Eqn. 14 [29, p. 477].

$$\frac{G}{T} = G_{rx} - T_{sys} \tag{14}$$

In Eq. 14, G/T is the receiver gain to noise temperature, G_{rx} is the receiving antenna gain, and T_{sys} is the system noise temperature. Using G/T, the total losses in the system, and EIRP one can determine the receiver carrier to noise ratio [29, p. 477].

$$\frac{C}{N_0} = EIRP + \frac{G}{T} - L_{total} + 228.6 \tag{15}$$

Using the value from Eq. 15 and the data rate in decibels, one can calculate the energy per bit to noise ratio [29, p. 478].

$$\frac{E_b}{N_0} = \frac{C}{N_0} - R_b \tag{16}$$

(a) Best Case Communication   (b) Worst Case Communication
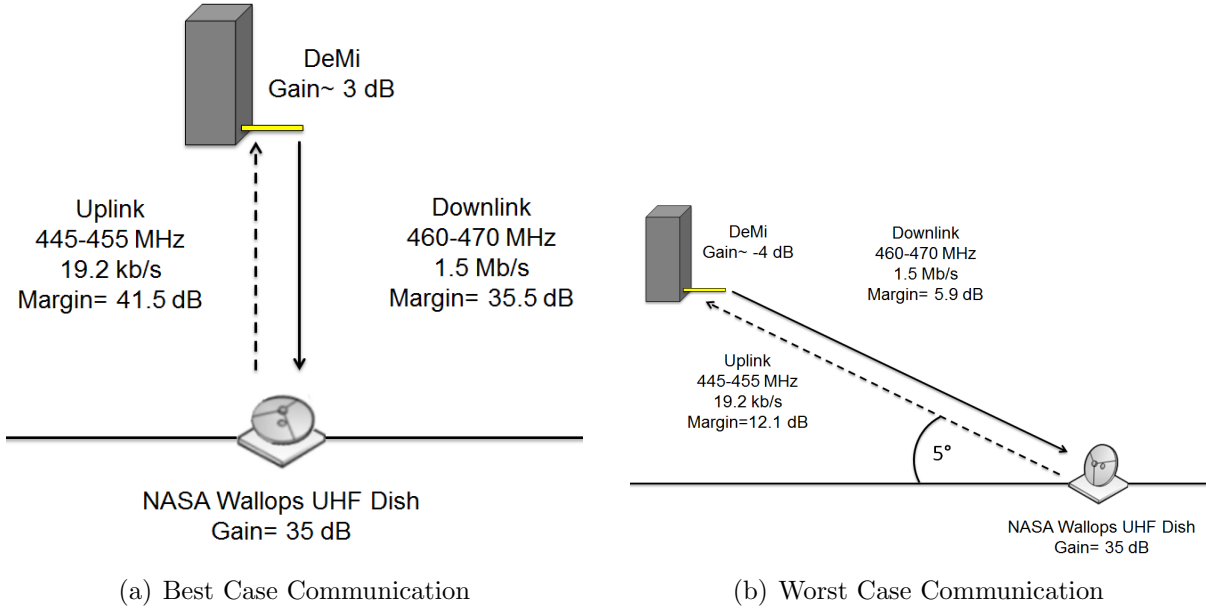
Figure 17: Representation of Satellite and Ground Station during a.) Best Case Communication and b.) Worst Case Communication

Finally, the link margin can be determined by subtracting the required energy per bit to noise ratio from the predicted one [29, p. 478]. The best and worst case link margins for uplink and downlink are shown in Figure 17.

3.3.5   Summary of Outputs - ZC

There were several outputs during the design process from the communications subsystem. These outputs include the ground station to the orbits subsystem, which is NASA Wallops UHF Ground Station, the beam width of Wallops UHF Ground Station and DeMi to ADCS, which are 2.9° and 65° respectively. The operational and survival temperatures of the transceiver to the thermal subsystem, the power for each mode to the power subsystem, and the mass and volume to the structures subsystem are detailed in Table 8.

3.3.6   Risks - ZC

Initially, there were concerns that communications may not be able to downlink enough of the data from the payload; however, avionics has decided that because of this risk, DeMi will be doing on-board processing so that less data is required to be downlinked. There is the risk that there may be a lot of interference at the frequencies that DeMi uses. In order to determine this, there would have to be a ground station site survey and if there were a problem with interference, specialized receiver software would have to be developed to mitigate the issue.

Table 8: Communications Budgets

Output	Value
Power (Standby)	0.51 W
Power (Data Capture)	0.51 W
Power (Downlink)	11.44 W
Power (Uplink)	0.51 W
Power (Safe Mode)	0.51 W
Mass	$\sim 0.235\ kg$
Volume	0.069 U
Operating Temperature Range	$-20°$ to $70°$
Survival Temperature Range	$-40°$ to $80°$

3.3.7 Future Work - ZC

Moving on from here, the main thing that should be done is testing of measuring tape antennas. There is currently not very much information out there that is available to DeMi concerning them, so research to determine the exact gain, beam width and radiation patterns should be conducted.

3.4 Avionics

3.4.1 Requirements - VE

The Avionics subsystem requirements are presented in Appendix A. The main driving requirements are number 3 and 2 in the order of importance because they are the most challenging to satisfy with a current level of technology.

3.4.2 Trade Studies - VE

We have two main options that are able to satisfy the requirements for Avionics subsystem. Both are shown in Table 9

Table 9: Hardware Options

	Processing on-board	Raw images to the ground
Component Name	The Steepest Ascent Mission Interface Computer CS-MIC-G-EM	Single Board Computer Motherboard + PPM with TI MSP430F2618
Power Consumption	0.5 − 1.25 W	10 mW
Capabilities	Telemetry/Telecommand + Real time image processing on FPGA	Telemetry/Telecommand
Storage Capacity	Up to 16 GB	Up to 2 GB
Processors	TI MSP430 + Xilinx FPGA (model can be selected)	TI MSP430F2618
Interfaces	I2C, SPI, UART	I2C, SPI, UART
Mass	62 g	88 − 114 g

Since we have identified the Payload driven requirements as the most challenging, we have to start selection of appropriate hardware from that.

Table 10: Payload image capturing modes

Mode	640x480 px subframe	640x480 px subframe	1280x1024 px full frame
Frame Rate	100 fps	10 fps	10 fps
Data Rate	310 $Mbit/s$	31 $Mbit/s$	131 $Mbit/s$
Duration	30 s	300 s	60 s
Memory Required	1.14 GB	1.14 GB	0.96 GB

Lets consider approach when we downlink all the data generated by the Payload without processing it. From Table 10 we can see that Payload will be generating around 1 GB of data

every time it is run. For a given 1.5 $Mbit/s$ downlink speed in this case we will need 600 s to downlink all the data captured or 10 ground accesses. Since we have only one ground access every three orbits in general this particular approach seems to be too ineffective in terms of Payload active time.

Thats why we mainly consider the second approach when we do all necessary calculations onboard and send only results to the ground. It dramatically reduces the amount of transferred data to around $10 - 100$ KB instead of gigabytes and enables to implement a closed loop deformable mirror control system.

After we have solved a problem with data storage we can focus on the core of every Avionics subsystem - its processor. Now we have higher but still reasonable requirements for processing power according to the computation tasks that it will be solving: 1. Centroid, delta x and delta y, slope reconstruction, and 2. Linear algebra for mirror controller. The Steepest Ascent Mission Interface Computer CS-MIC-G-EM is a good fit for such tasks because it has an FPGA to be configured for image processing and a microcontroller for general tasks such as telemetry and ADCS computations.

3.4.3   Decisions Made - VE

We have made a decision to use CS-MIC-G-EM (Figure 18) mainly because it enables on-board image processing which reduces the amount of data we send to the ground and provides with a capability to build a closed loop deformable mirror control system.

Figure 18: Mission Interface Computer CS-MIC-G-EM [23]

It is also capable of providing the following interfaces with other subsystems see Table 11.

Table 11: Avionics hardware interfaces with other subsystems (*assuming update 10 times per second).

Subsytem	Component	Interface	Data rate
Payload	Detector (IDS UI-5241LE-M)	GbE	550 $Mbit/s$ max
	Mirror driver (BMC Mini-Driver)	USB 2.0	480 $Mbit/s$ max
	Laser (ThorLabs CPS 186)	GPIO	–
Power	EPS, PDM	12C	400 $Kbit/s$ max
ADCS	5 sun sensors	analog	100 bit/s*
	ADIS16305 IMU/Magnetometer	SPI	160 bit/s*
	Torque coils	12C (via PDM)	–
Thermal	14 Temperature Sensors	analog	100 bit/s*
	Thermal Heater	12C (via PDM)	–
Communication	Cadet NanoSat UHF Radio	RS232	1.5 $Mbit/s$

3.4.4   Analysis - VE

The system architecture in general is shown in Figure 19. The Mission Interface Computer we have selected allows us to separate telemetry from image processing data. The first is processed on CPU while the latter is done on FPGA.

3.4.5   Summary of Outputs - ZC

The Avionics system had very few outputs to the other subsystems. It had to give values to Thermal for operational temperature range for the computer which is $-25°$C to $85°$C. The survival temperature is unknown. It also had to give outputs to power for power consumed during the different modes, and to structures for the mass and volume. These outputs, or budgets are detailed in Table 12.

Table 12: This is a summary of the mass totals, power needs, and thermal needs of the avionics system.

| Output	Value
Power (Standby)	0.5 W
Power (Data Capture)	1.25 W
Power (Downlink/Uplink)	0.5 W
Power (Safe Mode)	0.5 W
Mass	0.062 kg
Volume	0.104 U
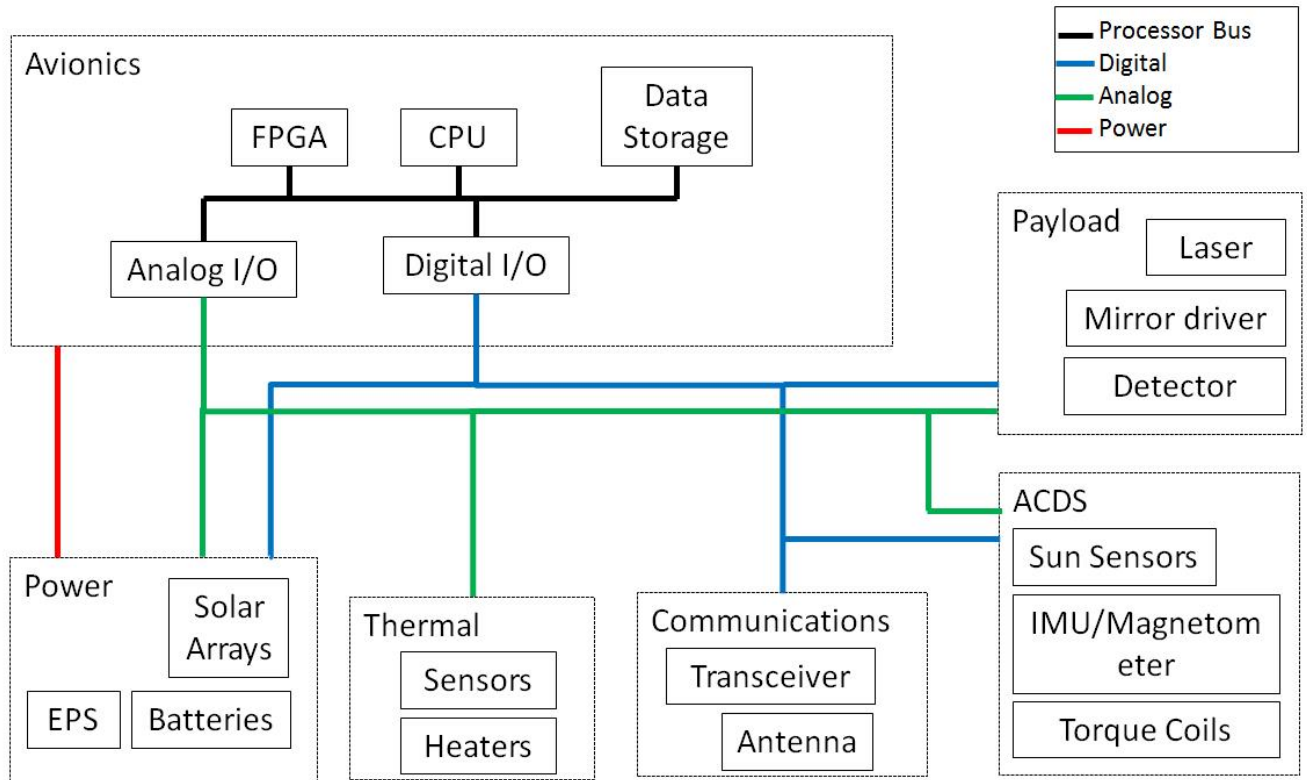
Figure 19: Caption goes here...

3.4.6 Risks - ZC

There are two risks that avionics faces currently. One risk which is a high consequence, but a very low likelihood is that the system will not be capable of processing all of the incoming data for payload. Payload is outputting a lot of data, and because the design of the code that will do the process has not yet been done, it is unclear how quickly Avionics will be able to process incoming data. The other risk that Avionics is currently faces, which is of very low likelihood, but very high consequence, is that it will not be capable of providing the required latency for Payload or for ADCS. Research needs to be conducted to determine how fast avionics can receive and issue orders to ensure that the computer is fast enough for the system. If it is not fast enough there could be major failures in the system because the attitude of the craft is not correct.

3.4.7 Future Work - ZC

The future work that needs to be conducted is that there should be work done to determine a new solution to interfacing with Payload. The mirror driver interfaces with USB 2.0, however the computer is not able to interface with this. So work should be done into determining how to resolve this. One other thing that should be looked into is ensuring that the system

can run all of the necessary calculations at the required speed so that all of the payload data can be processed and sent to the ground. If all of the data cant be processed, it would be difficult to complete our science goals.

3.5 Attitude Determination and Control System (ADCS) - TN

3.5.1 Requirements

The driving requirements of the ADCS design is shown below. A complete requirement document can be found in Appendix A.

- ADCS-1.1 ADCS shall meet 4.7 arcmin/s [TBR] slew rate requirement of payload imaging technology during external source science operation mode

- ADCS-2.1 ADCS shall provide attitude knowledge of the satellite to an accuracy within $10°$[TBR] for communication operations.

- ADCS-2.2 ADCS shall provide attitude control of the satellite to an accuracy within $15°$ [TBR] for communication operations.

- ADCS-3 ADCS shall provide momentum capability to despin upon launch vehicle separation within 30 days.

The two main requirements during operation modes for the ADCS subsystems are the pointing requirement ($15°$) for communication purpose and the stability (slew rate) requirement ($0.08°$/s) for the payload operation while imaging an external source. This requirement exists to ensure that a photon from the external source stays on the same pixel of the detector during data capture. In addition, the satellite is required to detumble and establish ground station access within a reasonable time frame. This duration is required to be less than 30 days, creating a secondary requirement on the total detumbling time.

3.5.2 Decision Made

Control Method Active magnetic control was chosen for this mission due to the low mass and low power requirement and sufficient attitude control performance for both communication requirement and payload science operation. According to documentation on the attitude control system of the 1U CubeSat COMPASS-1 from the University of Applied Sciences, Aachen, Germany, 3 magnetic coils of magnetic moment of 0.097 Am^2 can achieve a pointing accuracy of $8°$ [27]. The torque coils can be sized to generate enough torque for a 3U CubeSat. The details of this calculation will be presented in the torque coil specifications and analysis sections below. The stability of this control method is estimated to be $< 0.12°$/s, according to the Illinois Observing Nanosatellite (ION) 2U CubeSat from the University of Illinois [28]. The implementation of the active magnetic control the ION mission only includes magnetometer as sensor with low magnetic moment in each torque coils. The performance of the active magnetic control method is expected to improve significantly with the use of more accurate sensors, such as an inertial measurement unit (IMU) and sun sensors, and torque coils with higher magnetic moment. More analysis and testing is needed to determine the stability of the system.

Orientation The satellite will be in nadir pointing orientation with the nadir face being one of the two 10 cm × 10 cm faces. This orientation can be easily achieved by active magnetic control through sending control commands based on sensors readings to the active actuators. The 3U structure of the satellite provides gravity-gradient stability along the long axis in the nadir pointing configuration. By placing an antenna on the nadir face, this orientation facilitates access to the ground station. The satellite will travel with a corner-first configuration, to optimize the amount of power acquired from solar panels (see power section for more details). The orientation of the satellite is illustrated in Figure 20 below.
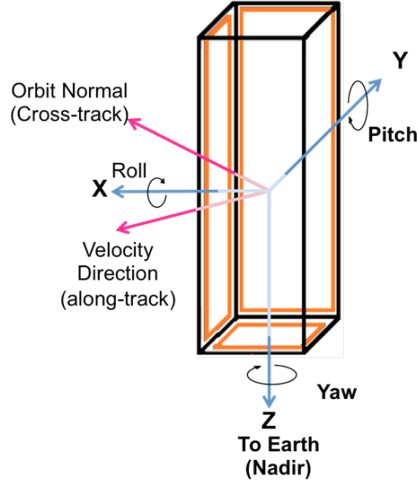

Figure 20: Satellite orientation with respect to nadir direction and velocity vector

ADCS sensors and actuators A summary of the sensors and actuators used in the ADCS is presented in Table 13 below.

Table 13: ADCS Sensors and Actuators

Sensors/Actuators	Quantity	Vendor	Performance	
Sun sensors	5	CubeSat shop	- Field of view: 114° - Accuracy: $< 0.5°$	
Magnetometer	1	Analog Devices (ADIS16405)	- Dynamic range: 3.5 gauss - Initial bias: 4 mgauss	
IMU	1	Analog Devices (ADIS16405)	- Dynamic range: 300°/s - Initial bias: 3°/s - In-run bias stability: 0.007°/s	
Torque coils	3	N/A	- Max magnetic moment: 0.060, 0.063 Am^2	

For attitude knowledge, a combination of sensors was chosen: sun sensors, magnetometers, and IMU. The sun sensors are low mass and low power attitude sensors that provides

accurate sun angle during day time, providing the orientation of the satellite relative to an inertial frame. Five sun sensors will be places on the faces of the satellite other than the nadir face. These sensors provides an accuracy of $< 0.5°$ and a wide field of view of $114°$. The magnetometer will be used to measure the local geomagnetic field to compute the magnetic moment needed to generate needed restoring torques. In addition, the magnetometer will be used as the main attitude sensing device during eclipse periods. An IMU is used to measure the angular rate of the satellite to provide more accurate vibration knowledge to yield a robust vibration damping control loop. The IMU and magnetometer are in the same sensor unit from Analog devices. Both sensors have initial biases that can be corrected for through computation.

For actuation, 3 custom-made orthogonal torque coils will be used for 3-axis stabilization control. The coils will be sized to meet the mass and power constraint of the satellite and to provide sufficient magnetic moment to counter environmental disturbances. More detailed calculation will be presented in the analysis section. The specifications of the torque coils are presented in Table 14 below.

Table 14: Torque coils specifications

Direction	Z	X, Y
Size	10 cm $\times$ 10 cm	10 cm $\times$ 30 cm
Quantity	1	2
Turns	500	300
Current	0.12 A	0.07A
Wire Gauge	28 AWG	28 AWG
Magnetic moment	0.60 Am^2	0.63 Am^2

System Schematics and Interfaces The system schematics are shown in Figure 21. The IMU/magnetometer unit, which will be mounted on an interface board, and the sun sensors will be read out through the analog channels of the power distribution module. The module will be used as an interface to the avionics subsystem. The attitude knowledge data will be processed in the avionics subsystem. Combining with the local magnetic field, the magnetic moment vector needed for the torque coils can be computed. This information will be sent to the torque coils through the Power Distribution Module (PDM), into the torque coil driver. The driver consists of a current driver and an H-bridge, which controls the current in each coils and their directions, respectively.

3.5.3 Trade Studies

Several control methods were considered in the design process of the ADCS system: passive magnetic control, passive magnetic control, and control using reaction wheels. The main
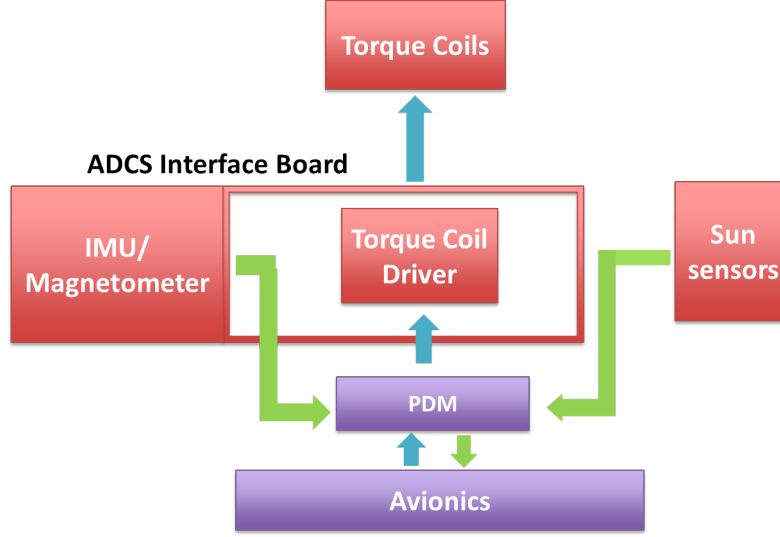
Figure 21: ADCS components interactions and Avionics interface

trades to be considered are mass, power usage, pointing accuracy, and pointing stability capability.

In passive magnetic control, restoring torque is generated through the alignment of the satellite magnetic moment with the local geomagnetic field. The magnetic moment is created through the use of permanent magnets. Hysteresis rods are used for vibration damping. This control option requires low mass and no power. Based on past CubeSat missions, the pointing accuracy of a passive magnetic control system in the same scale as DeMi can achieve $10°$ - $20°$, sufficient for communication requirement purpose [24] [25]. However, there are limitations in the ability to stabilize the satellite. Passive magnetic control systems stability performance is not reliable because the hysteresis rods do not provide fast and robust vibration damping. The expected stability achieved by this method is $1°$ - $10°/s$ [24]. Since the satellite will only have access to the external sources for a short amount of time, this method is not practical for capturing light from the stars. In addition, this control method limits the possible orientation of the satellite to only the direction along the local magnetic field. In a LEO orbit of $40°$ inclination such as that of DeMis, the direction of the local magnetic field varies at different orbital parameters. This variation causes difficulties in placing antenna and external source aperture so that ground station access and external source capture can be guaranteed.

Reaction wheels provide robust 3-axis stabilization control of the satellite. This control mechanism provides high accuracy ($0.0001°$ - $1°$) in pointing direction and quick response in vibration damping providing high stability ($0.05°/s$) [25]. However, the necessary sensors and actuators require high mass and power usage. The main mass contribution and power draw are from the reaction wheels. In addition, magnet torquers are also needed to desaturate reaction wheels, adding more mass and power strain on the system. This option is not practical for a small satellite such as DeMi.

43

A summary of the control methods performances is presented in table 15 below. Based on this information, active magnetic control was chosen for this mission.

Table 15: Performance of control methods considered in trade studies

	Passive Magnetic Control	Active Magnetic Control	Reaction Wheels Control
Mass	Low	Moderately Low	High
Power	Low	Moderately Low	High
Pointing Accuracy	$10° - 20°$	$1° - 10°$	$0.0001° - 1°$
Pointing Stabilization	$1°/s - 10°/s$	$< 0.12 °/s$	$< 0.05 °/s$

3.5.4 Analysis

Environmental Torque Calculation The main environmental disturbances on orbit are gravity gradient, magnetic field, aerodynamics drag, and solar radiation pressure. The governing equations of these external sources are presented in details in SMAD ADCS section [26]. Using the satellite properties, these values can be computed and presented in Table 16.

Table 16: Maximum Environmental Torque Estimation

Gravity Gradient	1.60E-08 Nm
Magnetic Field	1.80E-05 Nm
Atmospheric Drag	2.70E-07 Nm
Solar Pressure	5.50E-09 Nm
Total Torque	1.80E-05 Nm

Torque coil sizing calculation Magnetic control relies on the torque provided by the aligning of the satellite magnetic moment and the local magnetic field. Equation 17 shows the governing equation of magnetic control, where $\vec{T}$ represents the generated torque vector, $\vec{\mu}$ is the satellite magnetic moment, $\vec{B}$ is the local geomagnetic field vector.

$$\vec{T} = \vec{\mu} \times \vec{B} \tag{17}$$

Taking the torque vector to be the total environmental torque, Equation 17 yields the required maximum magnetic moment of the coils to be 0.6 A·m². The magnetic moment of each coil can be calculated from the coil parameters as shown in Equation 18 below, where

μ is the magnitude of the magnetic moment generated by the coil, I is the current in the coil, N is the number of turns, and A is the area of enclosed by the coil.

$$\mu = I \cdot N \cdot A \tag{18}$$

Since the area of each coil is chosen to be the same as the size of each of the face of the satellite, the main trade of the design is the number of turns and current in each coil. This corresponds to a mass/power trade. The results of the torque coil sizing are presented above in Table 14 in Decision Made section.

Detumbling Analysis   Using the Princeton Satellite Systems MATLAB simulation, the momentum unloading as a response to an initial angular rate can be computed. The input parameters are the magnitude and direction of initial angular momentum, the direction of magnetic moment, and the gain of the control loop. The initial momentum was calculated by assuming an initial angular rate. The magnetic moment direction is the direction of the torque coils. The control gain is adjusted so that the maximum magnetic moments along all 3 axes are less than the maximum magnetic moments provided by the torque coils. The detumbling time can be calculated through determining the time where the momentum in all direction is less than an arbitrary low threshold.

The simulation was run with an initial angular rate of $10°$/s, magnetic moment along x, y, z and a control gain of $k = 0.008$. The angular momenta and magnetic moments are presented in Figure 22.

The maximum magnetic moment needed in x, y, z are 0.6092 Am^2 , 0.6052 Am^2, 0.0938 Am^2, respectively, which is within the range of magnetic moment the torque coils can provide. The total detumbling time is less than 1 orbit (94 minutes).

Ground Access Duration   The duration of access to ground station was computed using an STK model. The orbit was set to a LEO orbit of 500 km altitude and an inclination of $40°$. The satellite configuration is set to be in nadir pointing with a possible offset of $8°$. The design of the antenna is a monopole antenna of 16 cm long (beamwidth of $65°$), transmitting at 465 MHz and receiving at 450 MHz. The corresponding length/wavelength ratio is 0.24. The ground station is set to NASA Wallops flight facility UHF parabolic dish of 18.29 m diameter (beamwidth of $2.9°$). A screen shot of the STK model is presented in Figure 23.

The simulation was run over the course of a day. There are a total of 5 access opportunities of about 9 minutes each. The total ground station access time per day is about 45 minutes. The exact access duration varies with each orbit.

3.5.5   Summary of Budgets

The mass, power, and volume budgets of the ADCS system are presented in Table 17. As expected, the main power draw and mass contribution of the ADCS system is from the torque coils. The power presented in the table (1.35 W) represents the power required by

45

Momentum Management: Momentum
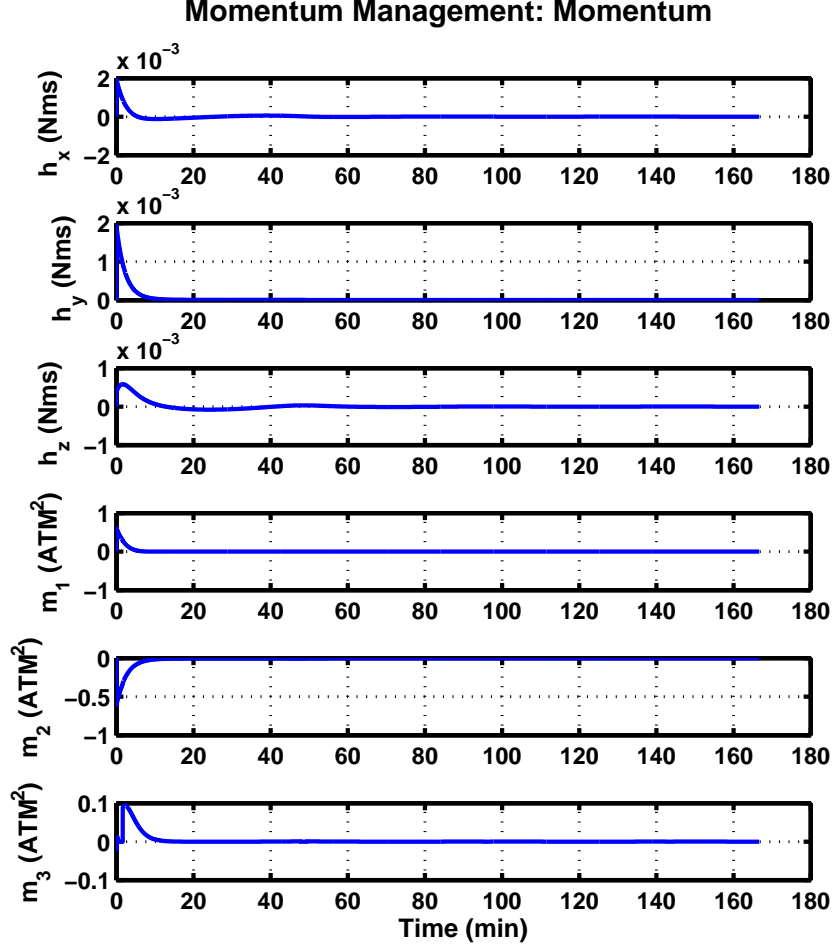
Figure 22: Momentum and magnetic moment during detumbling period

the actuators in the worst case scenario. The interface board takes up the most volume (0.318 U) and will stacked in the chassis along with the avionics boards.

3.5.6 Risks

The main design risk in the ADCS system is the pointing stability requirement and the mass and power budget. As previously mentioned, the stability of the satellite will need to be $< 0.08°/s$ for payload science operation of capturing light from a star. The sensors and actuators are expected to provide this performance based on the survey of past CubeSat missions. However, more analysis through simulation and testing will need to be implemented to determine the exact performance of the system. The second risk is due to the narrow margin on the power budget of the whole system. To compensate for this, the mass of the torque coils is higher than previously expected. More iterations are needed to determine the
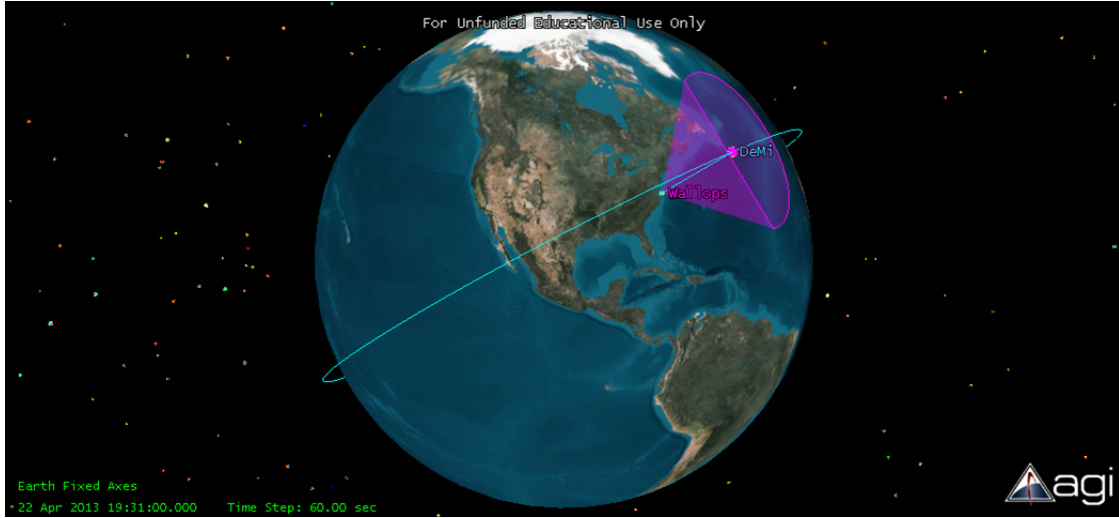
Figure 23: Ground access STK model

Table 17: ADCS budgets

Component	Volume	Mass	Power
IMU/Magnetometer	4.49 cm^3	0.016 kg	0.21 W
Sun sensors	6.530 cm^3	0.02 kg	0.25 W
Torque coils	58.32 cm^3	0.52 kg	1.35 W (max power)
Interface board	248.0 cm^3	0.17 kg	–

Total ADCS system (with margin)	318 cm^3 (0.318 U)	0.73 kg	1.81 W

optimal power consumption and mass of the torque coils.

3.5.7 Future Work

The main future work of the ADCS system is to simulate the flight condition through with external disturbance torques at each position on orbit. The next step is to create a control loop that takes these environmental torques as inputs to compute the needed magnetic moment of each of the 3 torque coils.

3.6 Thermal - David

3.6.1 Requirements

The requirements of the thermal subsystem were as follows:

- THM1: The thermal subsystem shall ensure that all components are kept within their survival temperature ranges for the duration of the mission.

- THM2: The thermal subsystem shall ensure that all operating components are kept within their operating temperature ranges.

- THM3: Monitor the temperatures of all key components.

3.6.2 Analysis/Results

The analysis of the thermal environment of the satellite took into consideration the radiation fluxes from the sun and earth (albedo and infrared) on all six faces of the cubeSat as shown in Figure 24. For each face, an energy balance was carried out and the average energy over all faces used to determine the average temperature of the satellite. The energy balance equations were are as follows:

$$Q_{in} + Q_{internal} = Q_{out} \rightarrow [\alpha(S + S_A) + \epsilon S_{IR}]A + Q_{internal} = A_S \epsilon \sigma T^4 \qquad (19)$$

Values for radiation flux over the course of an orbit were taken from the new SMAD, the main text for this course. Temperatures were calculated for two extremes, cold case, $\beta = 0$; hot case, $\beta = 45$, where β is the angle subtended by the orbit relative to the sun.
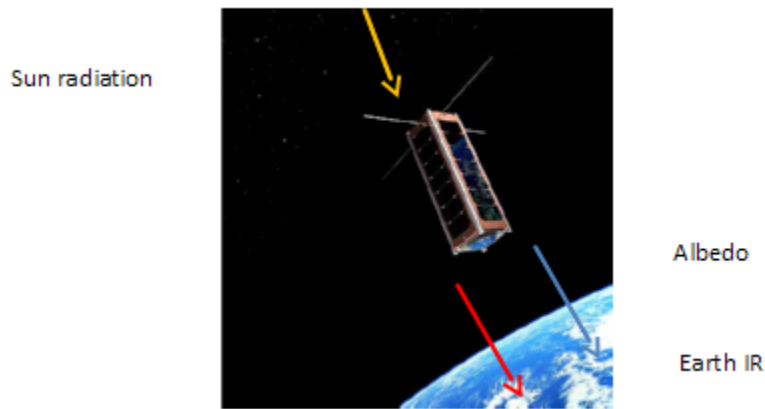

Figure 24: Thermal environment of satellite considered in analysis.

The operating and survival temperatures of other subsystems are shown in Table 18. These figures were used to determine the desired temperature range of the satellite during each mode of operation. The results of the analysis are shown in Table 19. These show

that during the cold case, the satellite will experience temperatures below the operation and survival temperatures of the payload during data-capture and other modes respectively.

Table 18: Operating and survival temperatures of different subsystems and components.

Equipment	Operating Temperature (°C)	Survival Temperature (°C)
Payload	0 to 35	-10 to 70
ADCS	-20 to 40	-20 to 40
Avionics	-25 to 85	-25 to 85
Batteries (have internal heaters)	0 to 50	-10 to 50
Solar Arrays	-40 to 80	-50 to 100
Communications	-20 to 70	-40 to 80

Table 19: Results of the thermal analysis for hot and cold cases.

Mode	Data Capture	Standby	Uplink	Downlink	Safe
Operating temp. (°C)	0 to 35	-10 to 40	-10 to 40	-10 to 40	-10 to 40
Temp. Cold case (°C)	-3.68	-13.40	-13.40	5.79	-15.72
Temp. Hot case (°C)	21.99	14.72	14.72	29.31	13.02

3.6.3 Trade Studies

Based on the results of the thermal analysis, the need to augment the thermal control was evident. Amongst the myriad of possible options, the inclusion of a heater, multi-layer insulation (MLI aka thermal blanket), and surface coating stood out as more feasible for a cubeSat mission given the limited mass, volume, and power available. Since the payloads detector was the main component whose temperature needed to be kept above the average satellite temperature for most modes of operation, a decision needed to be made on whether a heater or thermal blanket would be used as the primary thermal control for the payload.

The heater being considered was a model HK5586 polyimide thermofoil heater from Minco (see Figure 25). It takes up an area of 4.50 cm x 2.54 cm, operates within -200 to 200 °C, and with an input voltage of 3.3V, would require a maximum wattage of 0.83 W.

Computing the heat exchange between the heater and the detector, we obtained values for the average power required by the heater to keep the detector above 0 C during data capture mode, and above -10C during other modes. The equation used:

$$P_{req} = \frac{\text{Energy transferred}}{\text{Time}} = \frac{m_{sat}Cp_{sat}(T_{min} - T_{sat})}{\text{Time}} \tag{20}$$

Where a maximum of ten seconds is allowed for the detector to attain desired temperatures, and T_{min} corresponds to the minimum operational and survival temperature during
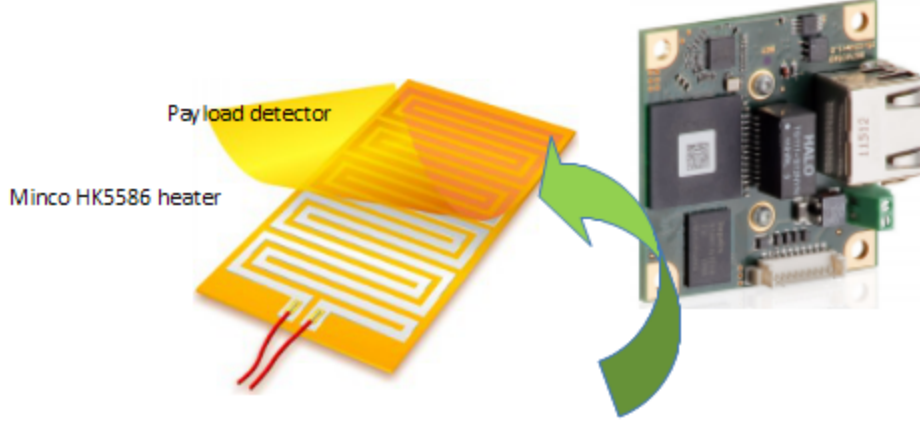
Figure 25: Thermofoil heater and payload detector.

data capture and other modes respectively. The results are shown in Figure 26. Excepting downlink mode, the heater will require power ranging from 0.44 to 0.75W, which is a significant percentage of the average power available to the entire satellite.

Figure 26: Power usage by heater during different modes of operation.

For the thermal blanket option, we considered aluminized 25 gauge polyester with nylon scrim from Dunmore. Some of the advantages of this option are that it does not require power, and its mass requirement is significantly low.

In order to determine the amount of insulation needed, a lumped parameter model for the thermal diffusion through the thermal blanket was used. Temperature of the inner face of the MLI is given by

$$T = T_\infty + (T_i - T_\infty)e^{-t/\tau}, \tau = m \times Cp \times R_{ext} \tag{21}$$

Where τ is the time constant for temperature decay, R_{ext} is the thermal resistance to external heat flux, and T_i and T_∞ are the initial temperature of the inner face and average temperature of the satellite respectively. In order to achieve a time constant of approximately the duration of eclipse, two layers of insulation will be required. The results are shown in Figure 27.

Figure 27: Temperature decay of inner face of MLI for different modes of operation.

3.6.4 Design/Budget

Given the results of the aforementioned analysis, the thermal blanket was chosen for primary thermal control. Initially, the thermal subsystem chose dispense with idea of a payload

heater, and use solely the MLI for thermal control, but after further discussion with other subsystems, it was agreed upon to still have the heater installed. The rationale behind this decision was that in the event that the average satellite temperature falls below the predicted value, the heater would be used to augment the action of the thermal blanket.

Thus, the design will include a double layer thermal blanket surrounding the payload, aluminized 25 gauge polyester with nylon scrim taking up approximately 1g and 0.8cm^3 of mass and volume respectively. In addition, the heater will be attached to the detector within the thermal blanket as shown in Figure 25.

Furthermore, in order to fully meet the third requirement of the subsystem, the temperatures of key components of other subsystems will be monitored via thermal sensors. These components are listed in Table 20 below.

Table 20: Key components and their corresponding number of thermal sensors required.

KEY COMPONENTS	Sensors needed
Sun sensors	5
Torque coils	3
ADCS interface board	1
DMs + Driver	1
Detector	1
Laser	1
Electronic Power System	1
Power Distribution Module	1
Total	**14**

The thermal sensors chosen are model 44004 precision thermistor elements from Omega, each of volume 0.04cm3 and mass 0.4g. Fourteen in all, they will each draw power of about 0.5 W and operate within a temperature range of -80 to 120 C. As shown in Figure 28 they consists of a bead and a tail; the bead will be attached to the surface of the component whose temperature is being measured, and the tail goes to the avionics board.

Figure 28: Precision Thermistor elements model 44004 (Omega.com).

In addition, the zenith and nadir faces will be painted with Chemglaze Z306 ($\alpha = 0.98, \epsilon = 0.89$) in order to improve their absorptivity-emissivity ratio from 0.9 to 1.1.

In summary, the mass, volume, and power budget will be as shown in Table 21

Table 21: Outputs (mass, power consumed, volume) to other subsystems.

	Mass (kg)	Power (W)	Volume (U)
Thermistors			
MLI			
Heater			
Surface coating			N/A

3.7   Structures

(See separate document.)

4   Conclusion - AW

In this report, it has been shown that a low-cost, quick-access mission can be carried out on a 3U CubeSat platform in order to demonstrate MEMS deformable mirror technology on-orbit. Continued iterations of the system design based on the current system risks and outlined in the section on future work need to be carried out in order to optimize the design.

4.1   Risk Summary

Although at this stage in the design the DeMi demonstration system supports a functional, on-orbit test of the deformable mirror technology, the mission is still confronted with a number of risks. Due to the fact that there is only a 9% margin instead of an 18% margin between the power required and the power that can be supplied to the system, there is a high consequence, medium likelihood risk (PO1) that there will not be enough power to supply the system in order to carry out the mission.

There is also a risk (S1) that the center of mass of the structure could move out of range. With the current design, the center of mass is within range. However, there still exists the possibility that masses and positions of the parts may change, the center of mass could potentially move out of range. This risk is low likelihood but high consequence.

Two risks exist regarding the avionics subsystem. The first, a low likelihood, high consequence risk (AV1), is that the avionics subsystem will not be capable of processing all of the incoming data. The second (AV2), regards the avionics system not being capable of providing the required latency for the payload and ADCS subsystems.

Additionally, there is a low consequence, low likelihood risk (AD1) that ADCS will exceed the system mass budget. Since a trade between mass and power was made in the design of the torque coils, both the mass and power budgets of the system are tight. Additionally, the system components and design still have the potential to change in this stage of the design. Therefore, if the torque coil design needs to change in order to reduce the power draw of the system, the mass might increase to above the maximum set by the CubeSat regulations.
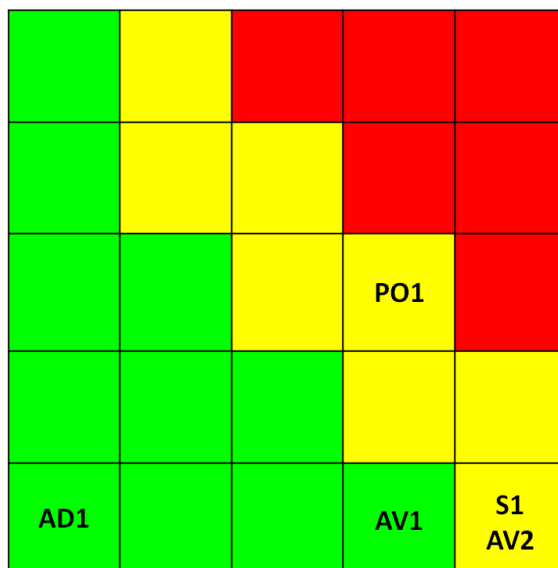
Figure 29: Systems level risk chart.

However, this is a low consequence, low likelihood risk since currently the system mass is under the maximum for a 3U CubeSat with over a 30% margin.

4.2 Future Work

More iterations in the design process need to be carried out before the design can be completed. Future work for the DeMi demonstration includes creating more detailed models of the temperature dependence of battery and solar panel performance and the temperature gradient across the satellite in order to more accurately calculate the power that can be supplied to the system and to determine whether the proposed heating design will be effective. Additionally, as the design continues to mature, the structural model will need to continue to be updated with new parts and part positions. It also needs to be verified that the structure and components will survive the launch environment. In addition, further research needs to be conducted on the construction and use of the measuring tape antenna. More research and analysis needs to be carried out regarding the interface with payload and it must be confirmed that the avionics system can process all information at the required speed. Finally, ADCS needs to create more accurate models of external disturbances and an attitude control loop.

In this paper it has been shown that a low-cost, quick-access mission can be carried out on a 3U CubeSat platform in order to demonstrate MEMS deformable mirror technology on-orbit. Continued iterations of the system design based on the current system risks and outlined in the section on future work need to be carried out in order to optimize the design.

5 Acknowledgment

A   Requirements

DeMi Requirements

ID	Statement	Parent Requirement	Rationale	Verification Method	Revision date	Expert Contact
example	The system shall…	MLR-4	Mission goal, etc.	Analysis	2/15/2013	kerberosUserna
Mission Statement						
MS-1	The mission of the Deformable Mirror Demonstration (DeMi) is to provide a low-cost, quick access platform to demonstrate microelectromechanical system (MEMS) deformable mirror technology on orbit.				2/18/2013	zaira
Mission Level Requirements						
MLR-1	The system design shall follow a 3-unit CubeSat platform.	MS-1	Low-cost, quick access space platform	Inspection	2/23/2013	zaira, acarlton
MLR-2	The system shall primarily use commercial off the shelf (COTS) and CubeSat parts and components.	MS-1	Low-cost option for a university project	Inspection	2/23/2013	zaira, acarlton
MLR-3	The system shall accommodate and operate a MEMS deformable mirror demonstration experimental payload.	MS-1	Mission goal	Inspection	2/23/2013	zaira, acarlton
MLR-4	The system shall operate and produce operational and experimental data for a period of [TBD].	MS-1	Mission goal	Analysis	2/23/2013	zaira, acarlton
System Requirements						
SYS-1	The system shall survive launch conditions.	MLR-4	Safety and mission requirement	Testing	2/18/2013	zaira
SYS-2	The system shall include electrical, mechanical, and software interfaces to the payload.	MLR-3	Mission requirement	Inspection	2/18/2013	zaira
SYS-3	The system shall comply with the requirements and constraint listed in the most current CubeSat Design Specification (CDS) document.	MLR-1	CDS is the standard for CubeSat mission design	Inspection	2/23/2013	zaira
SYS-4	The system shall be capable of sending and receiving data and instructions to and from the ground.	MLR-3, MLR-4	Mission requirement	Testing	2/18/2013	zaira
SYS-5	The system shall have a deorbit time of 25 years or less.	MLR-4	Current regulation	Analysis	2/23/2013	zaira
ADCS Subsystem Requirements						
ADCS-1	ADCS shall meet payload performance requirements during external-source science operation mode				3/8/2013	
ADCS-1.1	ADCS shall meet 4.7°/s [TBR] slew rate requirement of payload imaging technology during external source science operation mode	MLR-3	Payload requirement	Lab testing, Analysis	3/8/2013	tamz, alewasse
ADCS-2	ADCS shall provide attitude knowledge and control during communication operation				3/1/2013	
ADCS-3.1	ADCS shall provide attitude knowledge of the satellite to an accuracy within [TBD] degrees for communication operations.	SYS-4	Communication requirement	Lab testing, Analysis	3/1/2013	tamz, alewasse
ADCS-3.2	ADCS shall provide attitude control of the satellite to an accuracy within [TBD] degrees for communication operations.	SYS-4	Communication requirement	Analysis	3/1/2013	tamz, alewasse
ADCS-3	ADCS shall provide momentum capability to despin upon launch vehicle separation within 30 days.	MLR-4	Detumbling requirement	Analysis	3/8/2013	tamz, alewasse
Avionics Subsystem Requirements						
AVI-1	Avionics shall provide the necessary interfaces to support all subsystems.	MLR-3, SYS-2	Required for operation	Lab testing	2/23/2013	zjcasas, dominicg
AVI-2	Avionics shall handle calculations required to run all subsystems in real time.	MLR-3, SYS-2	Required for operation	Lab testing	2/23/2013	zjcasas, dominicg
AVI-3	Avionics shall write and store data to a mass storage device onboard the satellite.	MLR-4, SYS-2	Data downlink not always available	Lab testing	2/23/2013	zjcasas, dominicg
AVI-4	Avionics shall permit software updates and be capable of reprogramming in orbit.	SYS-2	Reconfigurability	Lab testing	2/23/2013	zjcasas, dominicg
AVI-5	Avionics shall be able to recover from potential single event effects.	MLR-4	Required for operation in space environment	Analysis	2/23/2013	zjcasas, dominicg
Communication Subsystem Requirements						
C-1	The communications system shall provide the ability to transmit and receive data.	MLR-4, SYS-4	Mission requirement	Lab testing	2/27/2013	zjcasas, dominicg
C-1.1	The system at the satellite shall receive commands from the ground station, and transmit telemetry and image packets to the ground station.	C-1	Mission requirement	Lab testing	2/27/2013	zjcasas, dominicg
C-2	The communications system shall establish a robust and periodic link.	MLR-4, SYS-4	Required for operation	Lab testing	2/27/2013	zjcasas, dominicg
C-2.1	The system shall recognize correct packets from incorrect packets and request retransmission if the packet is faulty.	C-2	Maintain data integrity	Lab testing	2/27/2013	zjcasas, dominicg
C-2.2	The system shall store packets to prevent overflow.	C-2	Prevent data loss	Lab testing	2/27/2013	zjcasas, dominicg
C-2.3	The system shall identify missing packets and out of order packets.	C-2	Maintain data integrity	Lab testing	2/27/2013	zjcasas, dominicg

ID	Statement	Parent Requirement	Rationale	Verification Method	Revision date	Expert Contact
C-3	The communications system shall support a bandwidth and data rate necessary to transmit all telemetry and images.	MLR-4, SYS-4	Required for operation	Lab testing	2/27/2013	zjcasas, dominicg
C-3.1	The system shall transmit at [TBD] kbps for uplink and [TBD] kbps for downlink.	C-3	Abililty to link	Lab testing	2/27/2013	zjcasas, dominicg
C-3.2	The system shall have a bandwidth of [TBD] Hz for uplink and [TBD] Hz for downlink.	C-3	Ability to link	Lab testing	2/27/2013	zjcasas, dominicg
C-4	The communications system shall be able to encrypt data packets.	MLR-4, SYS-4	Required for uplink	Lab testing	2/27/2013	zjcasas, dominicg
C-5	The communications subsystem shall downlink data with a bit error rate no greater than [TBD]%.	MLR-4, SYS-4	Ensure continuous link during contact	Lab testing	2/23/2013	zjcasas, dominicg
C-6	The communications subsystem shall obey communications regulations.	SYS-5	Must comply with FCC, IARU regulations	Lab testing, inspection	2/23/2013	zjcasas, dominicg
Orbit Subsyste Requirem						
ORB-1	The orbit altitude shall sustain under aerodynamic drag for the duration of mission life time.	MLR-4	Ensure satellite remains on orbit for mission lifetime	Analysis	3/11/3013	tamz, alewasse
ORB-2	The orbit shall have an inclination of 40 deg. [TBR] for ground station access.	SYS-4	Ensure communication with ground station(s)	Analysis	3/11/3013	tamz, alewasse
Payload Subsyste Requirem						
PLD-1	The payload shall command a MEMS deformable mirror to run a pre-defined test sequence for at least 5 minutes [TBR] each orbit.	MLR-3, MLR-4	Mission requirement	Analysis	2/26/2013	acarlton, kree
PLD-1.1	The payload shall have the ability to control any combination of actuators within 0.001 seconds [TBR] of each other, at a minimum rate of 100 Hz [TBR], with a minimum stroke of 1.5 microns, and with a precision of at least 1 nm [TBR].	PLD-1	Need to be able to control individual actuators and the DM as a whole with a certain speed, rate, stroke, and precision	Lab testing	5/3/2013	acarlton, kree
PLD-2	The payload shall have the ability to measure and reconstruct the optical wavefront at one wavelength for the duration of a 5 minute [TBR] test sequence each orbit at a frequency of at least 10 Hz [TBR].	MLR-3, MLR-4	Need to be able to measure and reconstruct the wavefront in test our (theoretical) ability to correct for it.	Lab testing	5/3/2013	acarlton, kree
PLD-2.1	The payload shall have the ability to measure the optical wavefront at a minimum rate of 10 Hz [TBR] for at least one minute each orbit.	PLD-2	Diagnostic mode for taking full frame images	Lab testing	5/3/2013	acarlton, kree
PLD-2.2	The payload shall have the ability to measure the optical wavefront at a minimum rate of 200 Hz [TBR] for at least 30 seconds each orbit.	PLD-2	Burst mode for data capture	Lab testing	5/3/2013	acarlton, kree
PLD-2.3	The payload shall have the ability to reconstruct the optical wavefront with a minimum accuracy of 100 nm rms [TBR].	PLD-2	Need to be able to reconstruct the wavefront accurately	Lab testing	5/3/2013	acarlton, kree
Power Subsyste Requirem						
POW-1	Power subsystem shall supply 3.54 [TBR] watts to power bus on average over each orbit.	MLR-3	Satellite will not operate without power.	VirSat	5/1/2013	jclark, eremin
POW-1.1	Power subsystem shall have solar panels to supply power to other systems while satellite is in sunlight and recharge batteries for eclipse.	POW-1	CubeSat is too small for nuclear power to be worthwhile, and needs to run for long periods of time (i.e. needs to be able to recharge).	VirSat	3/1/2013	jclark, eremin
POW-1.1.1	Solar panels shall supply 3.54 [TBR] watts after 12 months [TBR] of operation.	POW-1.1	Need to supply sufficient power through end of mission.	VirSat	5/1/2013	jclark, eremin
POW-1.2	Power subsystem shall have rechargeable (secondary) batteries to supply power during eclipse.	POW-1	Satellite in LEO will spend up to 1/3 of its orbit in shadow, so we need to store power for that time.	VirSat	5/5/2013	jclark, eremin
POW-1.2.1	Secondary batteries shall have 2.1 [TBR] watt-hours of capacity after 12 months / 6,000 cycles [TBR].	POW-1.2	Batteries decay over time so we need enough capacity to support other systems through the end of mission lifetime.	VirSat	5/1/2013	jclark, eremin

ID	Statement	Parent Requirement	Rationale	Verification Method	Revision date	Expert Contact	
POW-2	Power subsystem shall supply 13.84 [TBR] Watt of power for peak operations	MLR-3	Power subsystem has to withstand maximum power draw.	Analysis and lab testing	5/1/2013	jclark, eremin	
Structural Subsystem Requirements							
STR-1	The primary structure shall be a 3U CubeSat.	SYS-3			3/18/2013	khoza, imdavid	
STR-1.1	The system shall be 340.5 mm in length (x) by 100.0 mm in width (y) by 100.0 mm in height (z)	STR-1	CubeSat design specification	inspection	2/25/2013	khoza, imdavid	
STR-1.2	The system shall not exceed 6.5mm in protrusion normal to the surface of the 100mm cube.	STR-1	CubeSat design specification	inspection	2/25/2013	khoza, imdavid	
STR-1.3	The center of gravity of the system shall be no more than 20 mm offset from centerline.	STR-1	CubeSat design specification	inspection	2/19/2013	khoza, imdavid	
STR-1.4	The structure shall be composed of Aluminum 7075 or 6061.	STR-1	CubeSat design specification	inspection	2/25/2013	khoza, imdavid	
STR-1.5	The system shall have rails of hard anodized aluminum.	STR-1	CubeSat design specification	inspection	2/25/2013	khoza, imdavid	
STR-1.6	The system shall pass a minimum of 1 fit check.	STR-1	CubeSat design specification	inspection	2/25/2013	khoza, imdavid	
STR-2	The structure shall provide space and attachment points for the payload, the avionics system, the power system, the ADCS, and the propulsion system.	SYS-1		inspection	3/18/2013	khoza, imdavid	
STR-2.1	Attachment points shall ensure no relative motion of attached modules during launch as well as during nominal operating conditions.	STR-2	Relative movement of modules could cause payload malfunction or other forms of malfunction	analysis and testing	2/17/2013	khoza, imdavid	
STR-2.2	The structure shall survive thermal expansion and contraction across a range of -150 degrees C TBR to 60 degrees C TBR.	STR-2	some temperature variation is inevitable	analysis and testing	2/23/2013	khoza, imdavid	
STR-2.3	Lowest resonant frequency of all CubeSat components shall be higher than resonant frequency of launch vehicle.	STR-2	if launch vehicle vibrations could hit resonant frequencies of the CubeSat, vibrations could result in system failures.	testing	2/17/2013	khoza, imdavid	
STR-3	The structure shall facilitate interfaces between other subsystems.	SYS-2	subsystems need to recieve inputs from and send outputs to other modules.	inspection	2/23/2013	khoza, imdavid	
STR-4	The structure shall support a mass of 4 kg including its own mass.	SYS-3	Mission goal	analysis and testing	2/17/2013	khoza, imdavid	
STR-5	Structure shall not allow induced magnetic fields to interfere with payload operation.	MLR-3	Mission goal	analysis and testing	2/17/2013	khoza, imdavid	
STR-6	Structure shall not interfere with payload field of view.	PLD-2	Mission goal, functionality of ACDS	analysis and testing	2/25/2013	khoza, imdavid	
STR-7	The structure shall allow for workmanship screening of avionics boards.	MS-1	decrease cost and likelihood of any mistakes made during manufacture	inspection	2/19/2013	khoza, imdavid	
Thermal Subsystem Requirements							
THM-1	The thermal system shall ensure that all components are kept within their survival temperature ranges for the duration of the mission.	SYS-2, MLR-3	Prevent component failure	Analysis and testing	2/25/2013	khoza, imdavid	
THM-2	The thermal system shall ensure that all operating components are kept within their operating temperature ranges.	SYS-2, MLR-3	Prevent component failure	Analysis and testing	2/25/2013	khoza, imdavid	
THM-2.1	The thermal system shall ensure that the payload operates in temperatures no higher than [TBD] degrees.	THM-2	Prevent component failure	Analysis and testing	2/25/2013	khoza, imdavid	
THM-2.2	The thermal system shall ensure that any batteries operate in temperatures no higher than [TBD] degrees.	THM-2	Prevent component failure	Analysis and testing	2/25/2013	khoza, imdavid	
THM-2.3	The thermal system shall ensure that the avionics system operates in temperatures no higher than [TBD] degrees.	THM-2	Prevent component failure	Analysis and testing	2/25/2013	khoza, imdavid	
THM-2.4	The thermal system shall ensure that the ADCS operates in temperatures no higher than [TBD] degrees.	THM-2	Prevent component failure	Analysis and testing	2/25/2013	khoza, imdavid	
THM-3	The thermal system shall be able to monitor the temperatures of all components.	SYS-2	Temperature data may prove invaluable for fault diagnosis	Testing	2/25/2013	khoza, imdavid	

DeMi Requirements						
ID	Statement	Parent Requirement	Rationale	Verification Method	Revision date	Expert Contact

B   Link Budgets

Figure 30: Uplink Budget

Item	Symbol	Units	Worst Case	Best Case	Source
				Uplink Budget	
frequency	f	GHz	0.45	0.45	Hardware
wavelength	lambda	m	0.667	0.667	Lambda=c/f
propagation path length	r	km	2082	500	Mission/ITU-R P.676-9 eq 17, 18, 19
data rate	R	bps	19200	19200	Hardware
data rate	R	dB	42.833	42.833	
transmit antenna diameter	D_t	m	18.29	18.29	Wallops
transmit antenna beam width	theta_t	deg	2.9	2.9	Wallops
transmitter power	P	W	1	2	from DICE mission
transmitter power	P	dBW	0	3.010	
transmit antenna gain	G_t	dBi	35	35	Wallops
transmit antenna pointing offset	e_t	deg	1	0	
transmit antenna pointing loss	L_pt	dB	1.5	0	Antenna Gain Pattern
transmitter line loss	L_l	dBW	1	0.5	Line Loss for Coax Cable <http://www.arrg.us/pages/Loss-Calc.htm>
equivalent isotropic radiated power	EIRP	dbW	32.5	37.510	SMAD 16-20
receive antenna efficiency	eta		0.5	0.5	approximate efficiency
receive antenna beam width	theta_r	deg	65	65	Antenna Gain pattern
receive antenna gain	G_r	dBi	-4	3	
receive antenna pointing offset	e_r	deg	5	1	SMAD
receive antenna pointing loss	L_pr	dB	3	0	
space loss	L_s	dB	151.884	139.494	SMAD 16-22
Dry-air and water vapor loss	L_atm	dB	0.02	0.02	ITU-R P.676-9 Figure 6
total loss	L_comb	dB	157.404	140.014	
Sky Temperature	T_sky	K	60	30	
Ground Temperature	T_ground	K	290	290	
Antenna Temperature	T_antenna	K	117.5	95	Pozar Eq
Receiver Temperature	T_receiver	K	3270	3270	Hardware
System Noise Temperature	T_s	K	3387.5	3365	Pozar Eq
System Noise Temperature	T_s	dB	35.299	35.270	
receiver G/T	--	dB	-39.299	-32.270	SMAD 16-27
Boltzmann constant	k_b	dB	-228.599	-228.599	--
C/N0	--	dB	64.397	93.826	SMAD 16-30
Eb/N0	--	dB	21.563	50.993	SMAD 16-31
Bit Error Rate	BER	%	10^-5	10^-5	
Required Eb/N0	--	dB	9.5	9.5	SMAD figure 16-16
margin	--	dB	12.064	41.493	SMAD16-33

Figure 31: Downlink Budget

Item	Symbol	Units	Worst Case	Best Case	Source
frequency	f	GHz	0.465	0.465	Hardware
wavelength	lambda	m	0.645	0.645	Lambda=c/f
propagation path length	r	km	2082	500	Mission/ITU-R P.676-9 eq 17, 18, 19
data rate	R	bps	1500000	1500000	Hardware
data rate	R	dB	61.761	61.761	
transmit antenna length	l	m	0.164	0.164	quarter-wave monopole
transmit antenna beam width	theta_t	deg	65	65	Antenna Gain Pattern
transmitter power	P	W	1	2	from DICE mission
transmitter power	P	dBW	0	3.010	
transmit antenna gain	G_t	dBi	-4	3	
transmit antenna pointing offset	e_t	deg	5	1	SMAD
transmit antenna pointing loss	L_pt	dB	3	0	
transmitter line loss	L_l	dBW	-1	-0.8	Line Loss for Coax Cable <http://www.arrg.us/pages/Loss-Calc.htm>
equivalent isotropic radiated power	EIRP	dbW	-6	6.810	SMAD 16-20
receive antenna efficiency	eta	--	0.5	0.5	approximate efficiency
receive antenna beam width	theta_r	deg	2.9	2.9	Wallops
receive antenna gain	G_r	dBi	35	35	Wallops
receive antenna pointing offset	e_r	deg	1	0	
receive antenna pointing loss	L_pr	dB	1.5	0	Antenna Gain pattern
space loss	L_s	dB	152.169	139.778	SMAD 16-22
Dry-air and water vapor loss	L_atm	dB	0.02	0.02	ITU-R P.676-9 Figure 6
total loss	L_comb	dB	155.689	138.998	
Sky Temperature	T_sky	K	290	290	
Ground Temperature	T_ground	K	60	30	
Antenna Temperature	T_antenna	K	232.5	225	Pozar Eq
Receiver Temperature	T_receiver	K	66	66	Wallops
System Noise Temperature	T_s	K	298.5	291	Pozar Eq
System Noise Temperature	T_s	dB	24.749	24.639	
receiver G/T	--	dB	10.251	10.361	SMAD 16-27
Boltzmann constant	k_b	dB	-228.599	-228.599	
C/N0	--	dB	77.161	106.772	SMAD 16-30
Eb/N0	--	dB	15.400	45.011	SMAD 16-31
Bit Error Rate	BER	%	10^-5	10^-5	
Required Eb/N0	--	dB	9.5	9.5	SMAD figure 16-16
margin	--	dB	5.900	35.511	SMAD 16-33

References

[1] Tyson, Robert K. and Benjamin W. Frazier. *Field Guide to Adaptive Optics*. Bellingham, WA: SPIE Press, 2012. Internet resource.

[2] Kay J., Kasdin, N. J., Belikov, R. *Wavefront correction in a shaped-pupil coronagraph using a Gerchberg-Saxton-based estimation scheme*, Astronomical Adaptive Optics Systems and Applications III, Vol. 6691, SPIE Proceedings, Washington, D.C., 2007.

[3] Cahoy, K. L., A. Marinan, B. Novak, C. Kerr, M. Webber. *Wavefront control in space with MEMS deformable mirrors*, Photonics West, MEMS Adaptive Optics VII, Vol. 8617, SPIE, Washington, D.C., 2013.

[4] Nicoletta, C. A. and A. G. Eubanks. *Effect of Simulated Space Radiation On Selected Optical Materials*. Washington, D.C.: National Aeronautics and Space Administration, 1972.

[5] Traeger, F., *Springer Handbook of Lasers and Optics.* New York: Springer, 2007.

[6] Demtroeder, W. *Laser Spectroscopy: Basic Concepts and Instrumentation*, 3rd ed. Berlin: Spring-Verlag, 2003.

[7] NPX NanoPositioning Linear Stages, Newport Corporation, URL `http://www.newport.com/NPX-Series-NanoPositioning-Linear-Stages/843084/1033/info.aspx` (visited May 10, 2013).

[8] Thomas, S., et al. "Comparison of centroid computation algorithms in a Shack-Hartmann sensor". *Monthly Notices of the Royal Astronomical Society*, MN-06-0231-MJ.R1, 2006.

[9] Tokovinin, A., (May 28, 2001). "Adaptive optics tutorial at CTIO" URL `http://www.ctio.noao.edu/~atokovin/tutorial/part3/wfs.html`, (visited 10 May 2013).

[10] MLA150-5C, ThorLabs Inc., URL `http://thorlabs.com/thorProduct.cfm?partNumber=MLA150-5C` (visited 5 May 2013).

[11] Boston Micromachines Corporation, ¡http://www.bostonmicromachines.com/light-modulator.htm¿ (accessed 5 May 2013).

[12] ZEMAX, Software Package, Ver. 13, Radiant Zemax LLC, Redmond, WA, 2013.

[13] Correia, C., H.-F. Raynaud, C. Kulcsar, J.-M. Conan, "On the optimal reconstruction and control of adaptive optical systems with mirror dynamics," JOSA A, 27(2), 333-349, doi:10.1364/JOSAA.27.000333 (2010).

[14] Greivenkamp, John E. *Field Guide to Geometrical Optics*, Bellingham, WA: SPIE, 2004. Print.

[15] Image from Clyde Space. URL `http://www.clyde-space.com/cubesat_shop/solar_panels_-_deployable`, (visited May 05, 2013).

[16] (2012). "CubeSat Kit – In Space." URL `http://www.cubesatkit.com/content/space.html`, (visited May 05, 2013).

[17] Strain, A, (February 14, 2011). "User Manual: CubeSat 3U Electronic Power System." URL `http://www.clyde-space.com/documents/2471`, (visited May 05, 2013).

[18] Worrall, K, (March 14, 2011). "CubeSat Power Distribution Module User Manual." URL `http://www.clyde-space.com/documents/2560`, (visited May 05, 2013).

[19] McLaren, V, (April 28 2010). "User Manual: Standalone 30Wh Battery." URL `http://www.clyde-space.com/documents/1902`, (visited May 05, 2013).

[20] (March 16 2012). "CubeSat Solar Panels." URL `http://www.clyde-space.com/documents/2625`, (visited May 05, 2013).

[21] "ITU-R P.676-9", URL `http://www.itu.int/dms_pubrec/itu-r/rec/p/R-REC-P.676-9-201202-I!!PDF-E.pdf`, (visited April 2013).

[22] Pozar, David M., *Microwave and RF Design of Wireless Systems*, Wiley, New York City, NY, 2001.

[23] Clyde Space. CubeSat Shop. [Online]. `http://www.clyde-space.com/cubesat_shop/obdh/364_mission-interface-computer-grande-em`, visited May 5, 2013.

[24] Sofyali, A. and Aslan, A.R. *Magnetic Attitude Control of Small Satellites: A Survey of Applications and A Domestic Example.* Istanbul Technical University. Istanbul, Turkey.

[25] Wertz, James, *Space Mission Engineering: The New SMAD*, Microcosm Press, Hawthorne, CA, 2011. pp. 578.

[26] Wertz, James, *Space Mission Engineering: The New SMAD*, Microcosm Press, Hawthorne, CA, 2011. pp. 570-573.

[27] Aydinlioglu, A. and Hammer, M. *COMPASS-1 Picosatellite: Magnetic Coils for Attitude Control.* University of Applied Sciences Aachen, Aachen, Germany.

[28] Gregory, S. *Attitude Control System Design for ION, the Illinois Observing Satellite.* Urbana, Illinois, 2004.

[29] Wertz, James, *Space Mission Engineering: The New SMAD*, Microcosm Press, Hawthorne, CA, 2011.